ABSTRACT

POLIT, SEBASTIAN. Development of a High Throughput Nano-Positioning System with Applications in Micro-Manufacturing. (Under the direction of Dr. Jingyan Dong).

This document consists of three different parts. The first one presents the design of a single degree-of-freedom high-bandwidth high-precision nano-positioning module for high-throughput nano-manufacturing applications. Compared with widely used lumped-compliance mechanisms (using notch flexure hinges) and distributed-compliance mechanisms (using compliant flexure beams), this nano-positioning module adopts a hybrid compliant-notch flexure-based structure. This flexure design decouples the performance requirements for the structural bandwidth and parasitic accuracy that are correlated in the lumped-compliance mechanisms and distributed-compliance mechanisms. The parallelogram hybrid compliant-notch flexure enables simultaneous achievement of a higher structural bandwidth and a smaller parasitic motion. The behavior of the nano-positioning module is analyzed theoretically with respect to its design parameters and performance objectives. Finite element analysis is also performed to study the dynamic responses and parasitic displacement of the designed nano-positioning module. The results from the theoretical and FEA analysis demonstrate the effectiveness of the hybrid compliant-notch flexure design over commonly used compliant mechanisms and notch flexure hinge based mechanisms, especially when a high structural bandwidth is required for high-throughput nano-manufacturing applications.

The second part is the development of a high throughput two dimensional nano-positioning stage using the previously developed nano-positioning modules as building blocks. Two nano-positioning modules are assembled together and two additional double clamped beams are integrated to the system in order to produce the desired device. The new integrated beams provide high stiffness to the system, while the hybrid modules decoupled the two axis displacement. As a result, a high bandwidth system that is capable of providing well controlled independent displacement in two dimensions is obtained. Theoretical analysis is presented to explain the design parameters and their effect in the system's behavior. FEA analysis is performed to simulate and optimize the system, and to confirm the results obtained in the theoretical analysis. Manufacturing and assembly processes are described and the manufactured final device is tested using high bandwidth piezoelectric actuator and capacitance sensors to complete the assembly. Static and dynamic responses are then experimentally tested and the desired high throughput required for the possible applications is verified.

Finally, a new micro-manufacturing application using the developed nano-positioning stage is performed. A proposal for a novel micro-milling process is presented and tested to verify the applicability of the developed nano-positioning system. Optimal machining parameters are suggested for specific given conditions, and a micro-machining methodology is developed. Then, different samples are machined to demonstrate the effectiveness of the proposed process in producing complex features with relatively high efficiency and quality.

The entire document shows the design of the one dimension nano-positioning modules as building blocks, their integration to develop a two dimension nano-positioning stage, and one of its possible applications in micro-manufacturing.

Development of a High Throughput Nano-Positioning System with Applications in Micro-Manufacturing

by
Sebastian Polit

A thesis submitted to the Graduate Faculty of
North Carolina State University
in partial fulfillment of the
requirements for the degree of
Master of Science

Industrial Engineering

Raleigh, North Carolina

2010

APPROVED BY:

_______________________________ _______________________________

Dr. Yuan-Shin Lee Dr. Yong Zhu

____

Dr. Jingyan Dong

Chair of Advisory Committee

BIOGRAPHY

Sebastian Polit was born in Quito, Ecuador on October 02th, 1977. He graduated from Metropolitano high school of Quito in 1995. He obtained his degree in Mechanical Engineering from the Escuela Politécnica del Ejército (ESPE), at Quito, in 2001. After graduation, he worked for a year as maintenance manager assistant in KFC Ecuador. Then, he worked 6 years as design engineer for CODIPLA (Construction, Design and Planning).

Following this work experience, he was awarded a Fulbright scholarship to pursue his Master of Science degree in Industrial Engineering in the department of Industrial and Systems Engineering in North Carolina State University.

ACKNOWLEDGMENTS

I would like to thank Dr. Jingyan Dong, my academic advisor, for his guidance and help, which have been of fundamental importance in the completion of this work. I would also like to thank the professors that have been part of my graduate education as teachers or through my research process. Thanks too to the laboratory personnel for all their help, advice and support.

I am grateful to the Fulbright Program and the Department of Industrial and Systems Engineering at North Carolina State University for the financial support that allowed me to pursue my Master's degree, and to enjoy this great academic and life experience. Thanks to all my friends that have been an important support during my years of study.

Thanks especially to my wife, Maria Cristina, without whose support this experience would have been very difficult to fulfill. To my parents, Diego and Margarita, my brother Nicolás, and all other members of my family for all the support received from the distance.

TABLE OF CONTENTS

LIST OF TABLES vi

LIST OF FIGURES vii

CHAPTER 1: INTRODUCTION 1

CHAPTER 2: Single degree of freedom nano-positioning module 5

2.1 Introduction 5

2.2 Comparison between different single degree-of-freedom flexure mechanisms 7

2.3 Analysis of hybrid compliant-notch flexure mechanism 11

2.4 Results from finite elements analysis 17

2.5 Application of the hybrid flexure modules 26

2.6 Conclusions 28

CHAPTER 3: Two degrees of freedom nano-positioning system 30

3.1 Introduction 30

3.2 Mechanical design and kinematic analysis 34

3.3 Structural and dynamic analysis 40

3.4 Design Considerations for a high-bandwidth stage ... 49

3.5 Finite Elements Analysis and Results ... 52

3.6 Experimental results ... 57

3.7 Conclusions ... 65

CHAPTER 4: Micro-milling using the designed hybrid two DOF nano-positioning stage ... 67

4.1 Introduction ... 67

4.2 Methodology ... 70

4.3 Set up and practical considerations ... 71

4.4 Machining variables calculations ... 74

4.5 Experiments results ... 76

4.6 Conclusions ... 80

CHAPTER 5: Conclusions and recommendations ... 82

REFERENCES ... 85

LIST OF TABLES

Table 1: Model parameters used in Figure 4: Dominant resonant modes for the three flexure configurations. 19

Table 2: Parameters combinations for visual surface quality tests. 77

LIST OF FIGURES

Figure 1: Different configurations of single degree-of-freedom flexure structures. (a) Lumped- compliance flexure. (b) Distributed-compliance flexure. (c) Hybrid compliant-notch flexure design. 8

Figure 2: Parameters for notch flexure hinges design 12

Figure 3: Illustration of the hybrid compliant-notch flexure mechanism. 14

Figure 4: Dominant resonant modes for the three flexure configurations. 18

Figure 5: Structural frequency vs. parasitic Abbe/sine error for different configurations...... 20

Figure 6: Modal shapes of 1st and 2nd modes. (a) 1st mode (3146 Hz) (b) 2nd mode (15512 Hz) 23

Figure 7: The maximum Von Mises stress with respect to displacement.............................. 24

Figure 8: (a) Stress distribution and (b) Stress distribution at a flexure hinge, (c) total displacement distribution (multiplied by 40). 24

Figure 9: (a) Two dimensional (XY) micro-positioning system. (b) Scheme of parallel kinematic XY stage design using parallelogram mechanisms [15]. (c) Another XY stage design with prismatic joints and parallelogram mechanisms [28]. (d) A high bandwidth XY stage implemented from scheme (c). 27

Figure 10: (a) Mechanical structure of the XY nanopositioning system (b) Schematic representation of the system (deformed system when x axis is actuated) (c, d) Equivalent linkage of the parallel kinematics XY stage for the purpose of analysis at the nominal position and under actuation. 34

Figure 11: Illustration of the hybrid compliant-notch parallelogram flexure module. 35

Figure 12: Stage displacement under different actuation force. 53

Figure 13: (a) Stress distribution of the deformed mechanism with deformation magnified by 100. (b) Stress distribution around the flexure hinges. 54

Figure 14: Vibration modes and their corresponding frequencies. 55

Figure 15: Out of plane displacement under Z load. 57

Figure 16: (a, c) Experimentally measured static displacement with respect to actuation voltage for one axis. (b, d) Cross-coupled displacement from the other axis. 58

Figure 17: Steady state noise level. 59

Figure 18: Noise histogram of steady state sensor measurements. 60

Figure 19: Frequency response of the nanopositioner. (a) From X actuator to X displacement. (b) X actuator to Y displacement. (c) Y actuator to X displacement. (d) Y actuator to Y displacement. 61

Figure 20: Closed-loop step response in X (left) and Y (right) directions. 63

Figure 21: Closed-loop stepwise motion. 64

Figure 22: Histogram of closed-loop steady state error.. 64

Figure 23: Set up for the proposed micro machining process. 72

Figure 24: Achieved surface finish compared with mirror like (#8). 78

Figure 25: Tool trajectory used in the G-CODE program. (a) Total surface trajectory. (b) Different considered sectors. 79

Figure 26: 2 x 10 um letters in a 50 um size square machined in aluminum using tungsten tip. 79

Figure 27: Array of half micron lines in a 50 um square... 80

CHAPTER 1: INTRODUCTION

Micro and nanotechnology have become increasingly important for the industry over the recent years. Broadly, the term nanotechnology means "*the study, development and processing of materials, devices and systems in which structure on a dimension of less than 100 nm is essential to obtain the required functional performance*" [1]. As a reference, the raw human eye can resolve features of around 20 um, it is $2x10^4$ nm. Nanotechnology is experiencing this fast development due to the high demand of low cost complex products with low requirements in energy and materials. Miniaturization is in fact an effective way to decrease the products' requirements for material and energy, and potentially lead to cheap production processes with almost no waste of resources.

Currently, nanotechnology has been applied to many increasingly important industries. For example, it is used in advanced optics to machine the mirrors used in X-ray telescopes that require nanometer accuracy. In addition, micro-features machined in integrated circuits are common in electronic industry. In a word, nanotechnology has been successfully applied to fields that go from aerospace industry, computer disks and semiconductor devices, to medicine, biotechnology and environmental protection industries.

For many applications in this broad field, from micro manufacturing to scanning and sensing, nano-positioning capabilities with high speed and submicron accuracy of motion are required. For example, scanning X-ray microscopes use high throughput micro-positioning stages to scan the sample surface [2]. In addition, high precision three degrees-of-freedom

nano-positioning systems (X, Y, θ) are required in submicron lithography [3]. In micro-machining in particular, atomic force microscopes (AFM) using high speed nano-positioners have been used to scratch metal surface at nanometer scale [4].

Some work has been done to develop high speed and accuracy micro-positioning stages. For instance, a novel parallel kinematic mechanism for integrated, multi-axis nano-positioning has been proposed in [5] and [6]. However, the continuously developing nano-scanning and nano-manufacturing applications for these devices in current industry, such as AFM scanners or nano-manufacturing through atomic manipulation, require throughputs that have not been achieved yet. For this reason, the development of novel devices that can achieve such characteristics is an active and important field of research.

In this document, the design of a new nano-positioning stage that can achieve the characteristics required for the modern micro-scanning and micro-manufacturing applications is presented and one of its possible specific applications is proposed. First of all, a novel nano-positioning hybrid module capable of achieving the required throughput for such applications is proposed. After successfully designed and tested, these new developed nano-positioning modules are used as building blocks for the development of a new multidimensional nano-positioning stage. Finally, with all the data obtained from extensive analyses and testing of this stage, the new system is proposed to be used in a specific application for micro-manufacturing.

For the first part, flexure structures and parallel mechanisms concepts are integrated to design the mentioned one degree of freedom (1 DOF) nano-positioning module. High speed and nanometer accuracy are the two main characteristics that this new design is focused on achieving. Theoretical analysis and FEM simulation are used to verify the effectiveness of this new design regarding the required characteristics.

In the second part, additional elements are integrated to these modules and are combined to generate a high throughput two degrees of freedom (2 DOF) nano-positioning stage. This new system is successfully designed, analyzed theoretically, tested through FEM simulation and finally experimentally tested in the laboratory. For the experimental tests, piezoelectric actuators and capacitance sensors are used to generate the desired displacement and register the obtained output respectively. The three used analyses, e.g. theoretical, FEM and experimental analyses verify the good mechanical characteristics of this new design. A closed loop configuration is also attempted using a DSP-based (Digital Signal Processing based) motion controller and the possibility of operating the new nano-positioning system in this configuration with good throughout is also verified.

For the last part, and as a possible application, the designed nano-positioning system is used in a new proposed manufacturing technique. A proposal of micro-milling using sharp tungsten tips as cutting tools, and the developed nano-positioning stage to generate the tool-sample motion is presented and the obtained results from practical experiments are used to verify the achievable speed, accuracy and quality of this new process.

The system is used to replace the traditional spindle used in normal milling that is a bottle neck when trying to miniaturize this process. The previously obtained experimental data are used to calibrate the system's trajectory and speed so that the recommended parameters to obtain the best possible surface finish under the experimental conditions (e.g. tip-sample material combination) are found for this new micro manufacturing technique.

CHAPTER 2: Single degree of freedom nano-positioning module

2.1 Introduction

Positioning with nanometer level resolution and accuracy is critically important for many modern technologies, especially in the fields of micro and nanotechnology. Micro/nano-positioning systems are widely used in various applications, such as optical alignment [7, 8], scanning probe microscope [2, 9], and micro/nano-manufacturing [3, 10, 11, 12, 13]. The majority of practical nano-positioners utilize flexure-based structures, such as compliant mechanisms and notch flexure-based mechanisms, due to their smooth and friction-free motion and high durability without wear and deterioration. Piezoelectric actuators and high resolution displacement sensors are widely used with flexure-based mechanisms to obtain displacement with nanometer level resolution. Among the flexure-based mechanisms, parallelogram mechanisms restrict all rotational degree-of-freedom of the connector (end-effector) and keep the connector parallel to the base, because of the equal lengths for their cranks and followers (the members connected to the base). In spite of rotation of the crank and the follower, the connector undergoes pure translation along a circular path. Due to this feature, the parallelogram mechanism can be directly used as a single degree-of-freedom nano-positioning module. Such nano-positioning modules can be easily configured as building blocks to build a multi-degree-of-freedom nano-positioner. The parallelogram mechanism has also been used in many other applications, such as delta–robots [14] and other low degree-of-freedom parallel kinematics nano-positioning stages [15, 5, 6, 16].

Structural frequency (open-loop bandwidth) becomes a critical requirement for the nano-positioner in high-throughput nano-manufacturing and metrology applications. Most of nanoscale manipulators and manufacturing processes have extremely fast speed. For example, the micro cantilevers that are used in scanning probe microscopes [17, 18, 19, 20, 21] and dip-pen nano-lithography [22, 23, 24] have bandwidths over 10-100 kHz. Fast manipulation and manufacturing processes place increasingly demanding performance requirements on nano-positioning systems. The slow response speed of nano-positioners (normally <500 Hz) becomes a bottle neck for achieving the high-throughput nano-manufacturing.

The structural bandwidth of the nanopositioner can be improved through increasing the structural stiffness and decreasing the mass of the flexure structure. However, for the widely used flexure-based structures, such as compliant mechanisms and notch flexure-based mechanisms, the bandwidth and accuracy does not scale well with the parameters of the flexure structures (e.g. their dimension and stiffness). Simply scaling up the dimensions of the flexure components will bring severe side effect (e.g. parasitic rotary motion of the end-effector). As the stiffness of the flexure-based mechanism is increased to achieve higher bandwidth, the parasitic motion of the system will increase as well, due to the undesired stress distribution and non-linear elastokinematic effects [25] over the mechanism when the dimension of the flexure components is scaled up. New concepts need to be developed for achieving high bandwidth and high-accurate nano-positioners.

In this chapter, a hybrid compliant-notch flexure-based single degree-of-freedom nano-positioning module is designed for achieving the desired mechanism with high structural bandwidth (i.e. natural frequency), while keeping the parasitic motion at a very low level. This flexure design decouples the performance requirements for the structural bandwidth and parasitic accuracy that are correlated in the lumped-compliance mechanisms and distributed-compliance mechanisms. The designed parallelogram hybrid compliant-notch flexure mechanism enables simultaneous achievement of a higher structural bandwidth and a smaller parasitic motion. Results from finite element analysis demonstrate the effectiveness of this hybrid compliant-notch flexure over widely used compliant mechanisms and notch flexure mechanisms, especially when a high bandwidth is needed from the flexure mechanisms. The resulted one degree-of-freedom nano-positioning modules can be used as building blocks for multi-degree-of-freedom (XY, XYZ) micro/nano-positioning and manufacturing applications. By assembling two or more nanopositioning modules together, customized multiple degrees-of-freedom systems can be built conveniently for variant applications.

2.2 Comparison between different single degree-of-freedom flexure mechanisms

Parallelogram four-bar linkages and parallelogram multi-linkages mechanisms are widely used in applications where the orientation of the effector needs to be fixed and the angular motion needs to be eliminated. Commonly used configurations for parallelogram mechanisms include lumped-compliance flexure systems (notch flexure hinges based systems) and distributed compliance flexure systems (compliant beam-based systems). However, such mechanisms do not scale well when high bandwidth is desired.

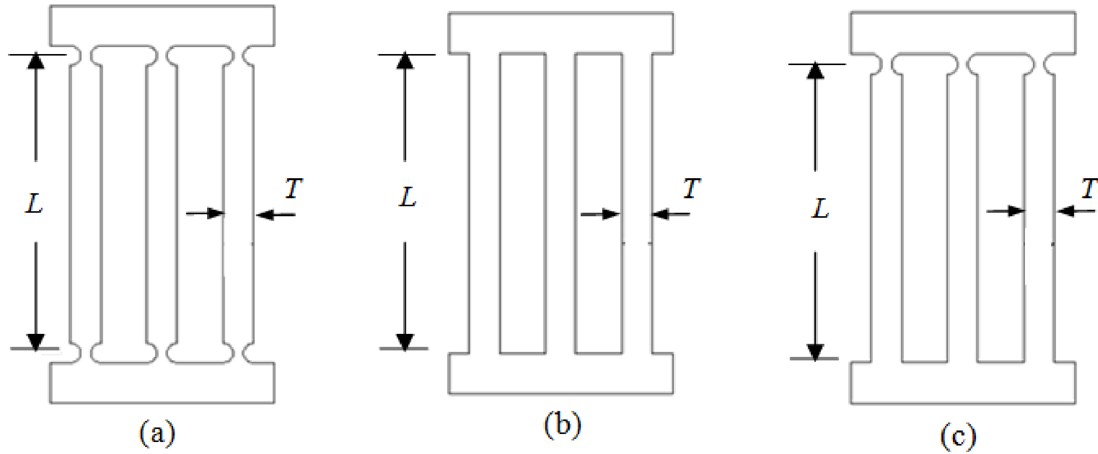

Figure 1: Different configurations of single degree-of-freedom flexure structures. (a) Lumped-compliance flexure. (b) Distributed-compliance flexure. (c) Hybrid compliant-notch flexure design.

As shown in Figure 1(a), the lumped compliance flexure consists of multiple parallel linkages that connect the connector to the base. Ideally, by using the parallelogram linkages, the connector only undergoes translational motion. In this configuration, the displacement of the mechanism is completely attributed to the rotational deflection of the flexure hinges that are treated as single axis rotary joints. This configuration helps to decrease the undesirable parasitic rotary motion due to the relatively easy kinematics obtained with the lumped compliance, especially when the flexure hinges can be treated as the ideal single-axis rotary joints. However, the natural frequency that can be achieved from this type of mechanism is generally not as high as other parallelogram flexure mechanisms, because the stiffness of the lumped compliance mechanism is provided purely by the flexure hinges, and lots of redundant mass (parallel linkages) does not contribute to the structural stiffness at all. An attempt to increase the structural bandwidth of the system is through increasing the thickness

of the flexure hinges, so as to obtain a larger structural stiffness. Although the main objective (high bandwidth) can be achieved in this way, the parasitic motion at the end-effector of the resulted mechanism will increase considerably, because the assumption that a flexure-hinge based joint is very close to an ideal rotary joint is not valid when the dimension of the flexure joint is too large. As a result, the natural frequency of the lumped-compliance flexure mechanism is increased at the cost of increasing the parasitic motion and sacrificing the positioning accuracy.

For the distributed compliance module (Figure 1(b)), there are no separate notch-flexure hinges. The structural stiffness is provided through the multiple parallelogram compliant beams, which is evidently an advantage considering the achievable structural frequency, because all the parallel compliant beam structures contribute to the stiffness of the mechanism. In addition, the mass of the system can be reduced based on the effective-mass theory that applies to the cantilever beams. As a result, the effective moving mass in the device is reduced, which results in a higher natural frequency. The multi-beam parallelogram flexure mechanism also provides better tolerance to the manufacturing error of its compliant components, due to the elastic averaging effect in the distributed-compliance mechanism [16, 25]. In spite of above advantages, the distributed-compliance mechanisms tend to produce a larger parasitic rotation (Abbe/sine errors) than the lumped-compliance mechanisms. Since there are no notch-based flexure hinges, the deformation comes from the compliance of the parallel beams. The deformation is nonlinear and coupled between the vertical and lateral directions. It is difficult to guarantee that the connector's orientation is exactly parallel to the

base. As a result, a large undesired parasitic rotation is generated. For this configuration, a high structural frequency can be achieved through increasing the width of the beam, *T*. However, larger beam width indicates larger nonlinearity in its deformation and larger parasitic motion. Generally, the distributed compliance configuration is capable of achieving a high bandwidth, but the parasitic motion is very large and the accuracy is not satisfactory.

A hybrid compliant-notch flexure-based mechanism is introduced in this chapter for simultaneous achievement of the high structural frequency (open-loop bandwidth) and the reduced parasitic error, as shown in Figure 1(c). The moving connector (end-effector) is connected to the base through circular flexure hinges followed by parallel compliant beams. Each linkage in the parallelogram flexure includes a compliant beam and a circular flexure hinge at the end of the beam. The parallel beams provide the high structural stiffness of the studied system, while the flexure hinges help to relief the undesired stress concentration at the end of the beams and make the connector orient to the base very well. The effective moving mass in this scheme is divided in two parts. The first part considers the effective mass of the parallel beams, and the second part considers the complete mass of the top effector. In this way, the hybrid compliance configuration is capable of achieving high structural bandwidth. With similar dimension of the flexural components, the bandwidth of the hybrid compliant-notch flexure-mechanism is comparable to that in the distributed compliance flexure-mechanism, but much larger than that in the lumped-compliance flexure-mechanism. Moreover, the parasitic rotations (Abbe/sine errors) of the end-effector are significantly lower than those from the distributed compliance flexure-mechanism, even

better than the lumped compliance flexure-mechanism when the bandwidth of the mechanism is high enough. The advantage of this hybrid compliant-notch flexure configuration is the decoupling of two contradicting performance specifications (i.e. structural bandwidth and parasitic Abbe/sine error). The hybrid flexure mechanism can be designed with high bandwidth (by increasing the beam width), and at the same time very small parasitic motion error (by decreasing the thickness of the notch flexure hinge) can be obtained. With this configuration, a device with high open-loop bandwidth and low parasitic motion error can be designed to satisfy the requirements of many high-precision and high-rate applications. The trade-off of this hybrid flexure design is its relatively small range-of-motion compared with the distributed compliance flexure mechanism, due to the large rotational motion of the notch-flexure-hinges in this mechanism required to obtain the same end-effector displacement. However, this disadvantage can be compensated by designing flexure-hinges with small thickness, so as to enlarge the maximum allowed rotational motion of the flexure-hinges and to increase the overall displacement range of the mechanism.

2.3 Analysis of hybrid compliant-notch flexure mechanism

In the hybrid compliant-notch-flexure-based mechanism, there are two types of compliant components: compliant beams and notch-flexure hinges. The hybrid design tries to incorporate the advantages of the distributed-compliance flexure mechanism and the lumped-compliance flexure mechanism to achieve the high structural bandwidth with low parasitic error. The stiffness of the hybrid compliant-notch flexure mechanism can be derived through beam theory, and the natural frequency can be estimated using the effective mass [26] of the

beams plus the mass of the top linkage. The stiffness of a single beam is described as follows:

$$k = \frac{EwT^3}{4L^3} \tag{2.1}$$

where E is Young's modulus of the material of the compliant structure, w is the device thickness, T is the beam width, and L is the length of the beam. Since the new design has multiple (3) beams as a multi-parallelogram structure, the overall stiffness is as follows: $K_b = nk = n\frac{\mathrm{EwT}^3}{4\mathrm{L}^3}$ and $n = 3$.

The design parameters for the single-axis circular flexure hinge are shown in Figure 2.

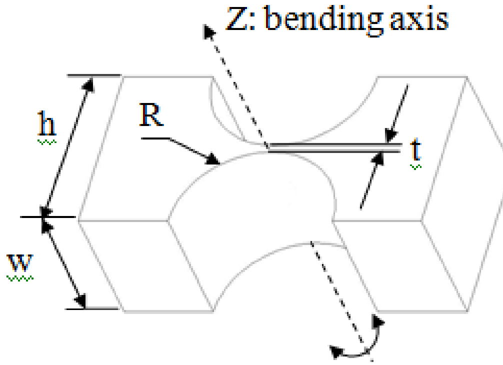

Figure 2: Parameters for notch flexure hinges design

The rotary compliance of the flexure hinge can be estimated by equation 2.2 from [27].

$$c_z = \frac{1}{k_z} = \frac{\alpha_z}{M_z} = \frac{3}{2EwR^2}\left[\frac{1}{2\beta + \beta^2}\right]x \tag{2.2}$$

$$\left\{\left[\frac{1+\beta}{\gamma^2} + \frac{3+2\beta+\beta^2}{\gamma.(2\beta+\beta^2)}\right].\left[\sqrt{1-(1+\beta-\gamma)^2}\right] + \left[\frac{6.(1+\beta)}{(2\beta+\beta^2)^{\frac{3}{2}}}\right].\left[tan^{-1}\left(\sqrt{\frac{2+\beta}{\beta}}x\frac{(\gamma-\beta)}{\sqrt{1-(1+\beta-\gamma)^2}}\right)\right]\right\}$$

Where $\beta = t/2R$; $\gamma = h/2R$; E is the Young's Modulus of the material of the flexure hinge; α_z is the angular deformation of the hinge about Z-axis in radians and M_z is the external bending torque applied to the flexure hinge. In the parallelogram mechanism, when the end-effector of the mechanism is actuated, all the flexure hinges undergo the same deflection, thus the rotary stiffness from the flexure hinges is $K_z = n\frac{1}{c_z} = nk_z$.

The overall stiffness of the mechanism can be derived through the principle of virtual work. The actuation force of the flexure mechanism not only displaces the parallel compliant beams, but also rotary flexure hinges at the end of the beam. In order to correctly predict the stiffness of the mechanism, the relationship between the end-effector displacement and the angular displacement of the hinges in the parallelogram mechanism has to be derived.

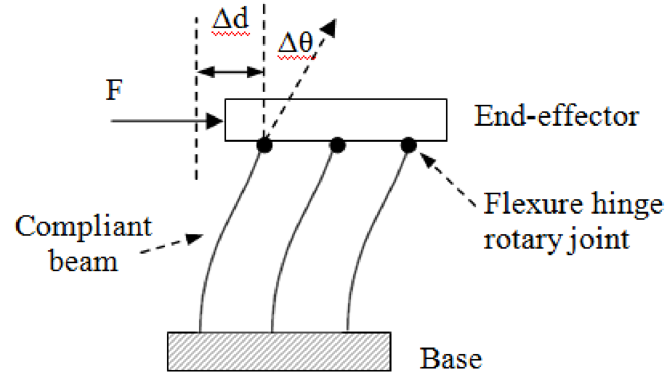

Figure 3: Illustration of the hybrid compliant-notch flexure mechanism.

As shown in Figure 3, a force is applied to the end-effector to generate a displacement of Δd at the end-effector and also at the tip of the parallel beams. Since the end-effector is parallel to the base, the flexure hinges absorb the rotary deflection of the cantilever beam, thus the rotational angle of the hinge is equal to the deflection angle at the tip of the beam. When the deflection is small compared with the size of the mechanism, which is the case for micro/nano-positioning, the beam deflection angle and the rotary angle of the flexure hinges is given [27] as follows:

$$\Delta\theta \approx \frac{3}{2}\frac{\Delta d}{L} \tag{2.3}$$

When the structure is actuated, the work done by the actuator is balanced by the energy stored in the beams and the flexure hinges. Using the principle of virtual work:

$$\frac{1}{2}F\Delta d = \frac{1}{2}K_b(\Delta d)^2 + \frac{1}{2}K_z(\Delta\theta)^2 \tag{2.4}$$

Here $\Delta\theta$ is the rotation angle of the flexure hinge. Simplifying equation 2.4 to express Δd in terms of the actuation force and flexure parameters, we obtain

$$\Delta d = \frac{F}{K_b + 2.25\,K_z/L^2} \tag{2.5}$$

The equivalent structural stiffness of the mechanism K_m is described by $K_m = K_b + 2.25\,K_z/L^2$. The maximum stress inside the compliant beams and the flexure hinges should always be kept within the proportional limit (yield strength) for the flexure mechanism to function properly. Such maximum stress imposes a limit on the maximum achievable displacement of the designed flexure mechanism. Since the flexure hinge has much higher stress concentration than the compliant beam, the maximum achievable displacement of the mechanism is generally limited by the maximum stress of the flexure hinges. The maximum stress inside the mechanism should be within its yield strength to avoid the plastic deformation of the compliant beams and hinges. Therefore the maximum bending torque that can be applied to a flexure hinge is:

$$M_{z-max} = \frac{2\sigma_p I_{min}}{t} \tag{2.6}$$

where $I_{min} = wt^3/12$, which is the smallest moment of inertia of the flexure hinge about the rotation axis; σ_p is the stress limit. The motion range limit of a flexure hinge $\alpha_{z-\max}$ and the maximum displacement of the mechanism $\Delta d_{\max}$ corresponding to the maximum bending torque are:

$$\alpha_{z-max} = M_{z-max} c_z \tag{2.7}$$

$$\Delta d_{max} = \frac{2}{3} \alpha_{z-max} L \tag{2.8}$$

For the new hybrid module design, the design parameters are shown in Figure 1(d) and Figure 2, where $t = 0.5mm$, $R = 1mm$, $w = 10mm$ and $L = 30mm$. Stainless steel is used to fabricate the micro-positioning module. The rotation limit of the rotary hinge is $\alpha_{z-max} = \pm 0.0038$ radians, which indicates a maximum motion range of 76 microns.

For the parallel cantilever beam, the maximum stress occurs at the fixed end with the maximum stress to be $\sigma_{max} = \sigma_p = \frac{6FL}{Tw^2}$. The maximum displacement that the beam undergoes before failure is:

$$\Delta d_{max} = \frac{2\sigma_{max} L^2}{3ET} \tag{2.9}$$

The beam design parameters are shown in Figure 1(d), where $T = 4.5\ mm$, and $L = 30mm$. The maximum motion range from the maximum stress concentration at the beam is about

160 microns, which is larger than the maximum displacement limited by the flexure hinge. The flexure hinge has a higher stress concentration than the compliant beam, and its maximum stress limits the maximum achievable displacement of the overall mechanism.

Using the derived structural stiffness, the resonant frequency of the mechanism can be estimated. In the flexible cantilever beam system, the effective mass is used to simplify the structural dynamic analysis. Similar idea of the effective mass can be used here to analyze the dynamic behavior of the hybrid compliant-notch flexure-based mechanism. The effective mass of the parallelogram linkage *is* $M_{eff} = c \times M_{link}$; here c is the coefficient of the effective mass with a numerical value 33/140 from [26]. The overall moving mass of the system includes the mass of the end-effector and the effective mass from the multiple parallelogram compliant beams, $M = M_{eff} + M_c$. The dominant resonant frequency can be express as follows:

$$f = \frac{1}{2\pi}\sqrt{\frac{K_m}{M}} = \frac{1}{2\pi}\sqrt{\frac{K_m}{M_{eff} + M_c}} \tag{2.10}$$

For this specific mechanism design, a theoretical resonant frequency about 3088.6 Hz is obtained.

2.4 Results from finite elements analysis

FEM (Finite Element Method) analysis is performed to verify the design objectives of the hybrid compliant-notch flexure-based mechanism, and to compare the differences among the

hybrid flexure mechanism, the distributed-compliance mechanism, and the lumped-compliance mechanism.

The finite element model of the designed mechanism has the boundary condition similar to the actual assembly. The base linkage is fixed in all directions. The actuation force is applied to the end-effector as shown in Figure 3. The FEM simulation is performed using COMSOL. The material of the mechanism is set to be stainless steel (AISI 302).

First, finite element analysis for the three different flexure configurations of the micro/nano-positioning module is performed to compare their performance with respect to the bandwidth and the parasitic motion. To evaluate the structural bandwidth capabilities, the dimensions for the flexure hinges and compliant beams used in the three flexure configurations are chosen to be the same, so as to give a fair comparison.

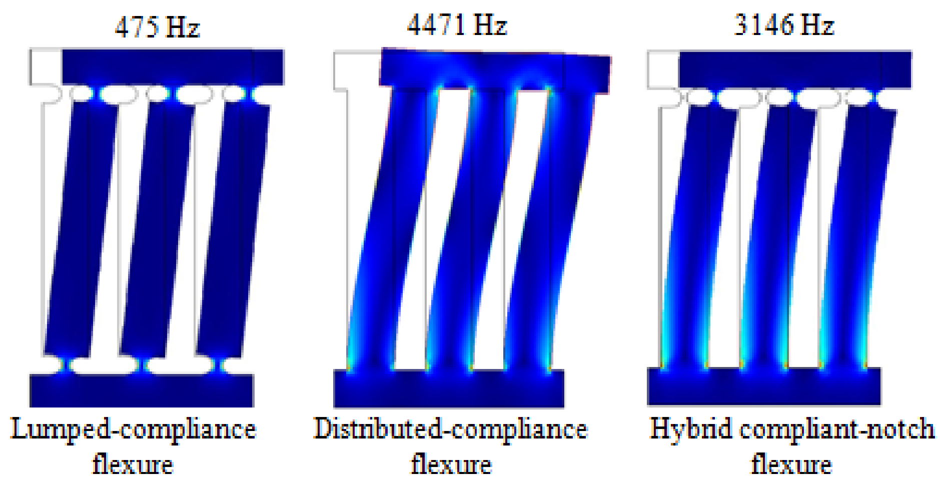

Figure 4: Dominant resonant modes for the three flexure configurations.

As shown in Figure 4, the hybrid flexural mechanism can achieve a much higher structural bandwidth than the lumped compliance module (> 3kHz versus 475 kHz), without increasing the parasitic Abbe/sine error.

Table 1: Model parameters used in Figure 4: Dominant resonant modes for the three flexure configurations.

Module configuration	*T (mm)*	*L(mm)*	*w(mm)*	*R(mm)*	*t(mm)*
Lumped Compliance flexure	4.5	30	10	1	0.5
Distributed Compliance flexure	4.5	30	10	n/a	n/a
Hybrid flexure	4.5	30	10	1	0.5

With the same flexure configuration, the distributed compliance flexure achieves the highest natural frequency, which can be explained by the different boundary conditions compared with hybrid flexural mechanism. In the hybrid flexural mechanism, due to the existence of the flexure hinges (rotary joints), the parallel compliant beams behave as free cantilever beams. However, in the distributed-compliance flexure, since the orientation at the end of the parallel beams is constraint by the end-effector, the parallel compliant beams act as guided cantilever beams (S-shape) with larger structural stiffness. But as it in shown in Figure 4 and Figure 5, the parasitic Abbe/sine error becomes unacceptable using this distributed-compliance configuration. The parasitic error can be identified as the orientation change of

the end-effector in the distributed-compliance flexure in, where the end-effector is no longer parallel to the base.

To demonstrate the scalability of the structural bandwidth in these three flexure mechanisms, the relationship between the obtained structural bandwidth and the other important design objective (i.e. accuracy or parasitic Abbe/sine error) of these flexure mechanisms are studied. By changing the design parameters of flexural components in these mechanisms (beam width *T* in the distributed-compliant flexure, hinge width *t* in the lumped-compliant flexure, and beam width *T* in the hybrid flexure for a fixed hinge width *t* (t=0.5mm. and t=1mm.)), the corresponding dominant structural frequencies through eigen-frequency analysis for all three flexure configurations can be obtained.

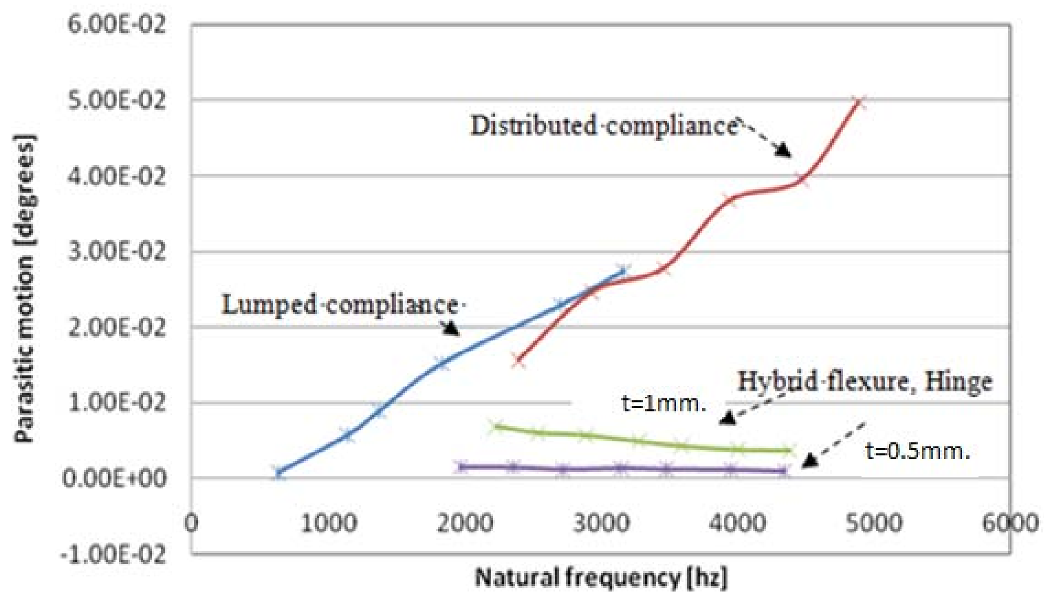

Figure 5: Structural frequency vs. parasitic Abbe/sine error for different configurations.

For each set of design parameters, an actuation force is applied to the mechanism to obtain a given displacement in the actuation direction. The parasitic Abbe/sine error is measured at the end-effector. Figure 5 demonstrates this relationship between the designed structural bandwidth and the corresponding parasitic rotation error (Abbe/sine errors) of the end-effector for these three flexure designs. In Figure 5, the higher structural bandwidth is achieved by increasing the size of the flexure hinge (for the lumped-compliance flexure) and the compliant beam (for the distributed-compliance flexure and the hybrid flexure mechanism). Clearly with a similar device volume, the achievable structural bandwidth of the lumped-compliance flexure is lower than the distributed-compliance flexure and the hybrid flexure, due to excess mass from the linkages. For the lumped compliance-flexure and distributed-compliance flexure, when the resonant frequency is scaled up, the parasitic rotational errors increase rapidly because of the nonlinear deformation and undesired stress distribution of the compliant components. In the hybrid flexure mechanism, the structural frequency is increased by enlarge the dimension of the compliant beams. The dimension of the flexure hinges is unchanged and is set at a range so that the behavior of the flexural hinges is still close to the ideal rotary joints. Such ideal rotary joints make the end-effector orient to the base very well and effectively decrease the parasitic Abbe/sine error. As the results, the hybrid flexure design gives extremely small parasitic error, as shown in Figure 5. The parasitic rotation error is almost independent from the structural bandwidth when the size of the flexure hinges is fixed. As we increase the size of the flexure hinge (hinge width t change from 0.5mm to 1mm), the parasitic rotation error get increased too, since the flexure

hinges become less like ideal rotary joints. But the parasitic rotation error is still almost constant and independent of the structural bandwidth. In other words, the two important performance specifications, structural bandwidth and parasitic error, are decoupled in the hybrid flexure design. This feature of the hybrid flexure mechanism becomes a big advantage over the widely used distributed-compliance flexure and lumped compliance flexure mechanisms, in which structural bandwidth and parasitic error are two conflicting performance requirements, and it is difficult to satisfy these requirements at the same time. With this advantage, the hybrid configuration provides the flexibility to be configured for simultaneously achieving the objectives of the high structural bandwidth and low parasitic error. The structural frequency can be improved through increasing the beams width, while the undesirable parasitic motion can be controlled by choosing the proper size of the notch flexure hinges.

Eigen-frequency analysis is performed using FEM to estimate the natural frequencies of the resulted hybrid flexure design. Figure 6 shows the first two dominant mode shapes for the system; different color indicates the different displacement in the vibration mode. The first mode (dominant mode) has a frequency of 3146 Hz which corresponds to the desired translational motion of the flexure module. This value is close to the structural frequency predicted by the theoretic analysis (3088.6 HZ). The second mode at a frequency of more than 15 kHz is related to the dynamics of a single compliant beam, and is difficult to be excited by the actuation effect.

The modal frequency is much higher (5 times) than the desired translational mode of the flexure module, which indicates much higher stiffness (25 times) to displace and excite such undesired motion.

The elastic operating range can be found from the maximum stress inside the flexure system. In Figure 7, the displacements obtained from the system by applying different driving forces are plotted against the maximum von Mises stress. From the Figure 7, considering the elastic limit of the material as 240 MPa, the maximum displacement that the system can achieve without producing plastic deformation is 71μm with an actuation force of 297 N.

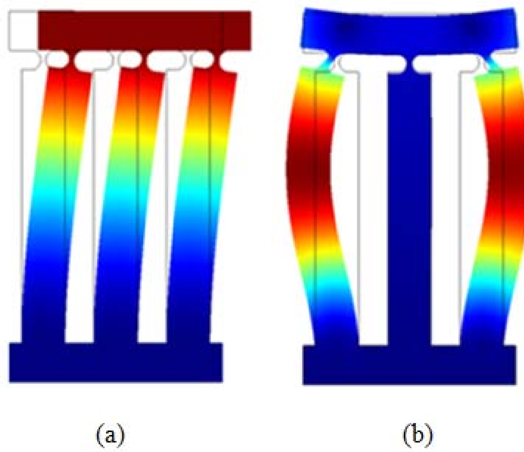

Figure 6: Modal shapes of 1st and 2nd modes. (a) 1st mode (3146 Hz) (b) 2nd mode (15512 Hz)

Figure 8 shows the von Mises stress and total displacement distribution over the structure when the maximum driving force is applied.

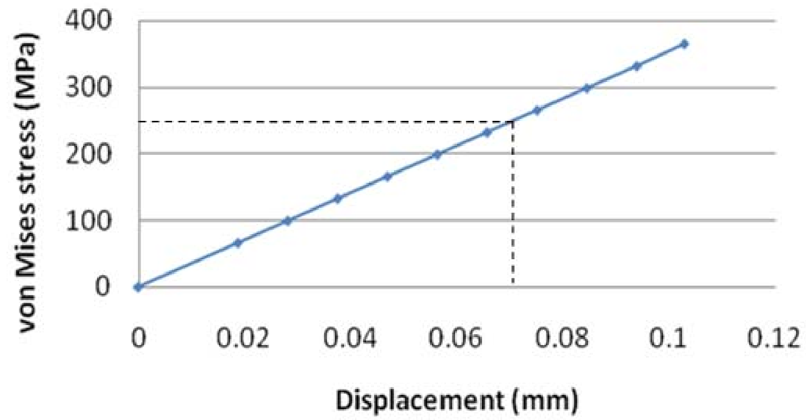

Figure 7: The maximum Von Mises stress with respect to displacement.

From the stress distribution it can be seen that stress concentration occurs in the hinge regions and along the edge of the compliant beams.

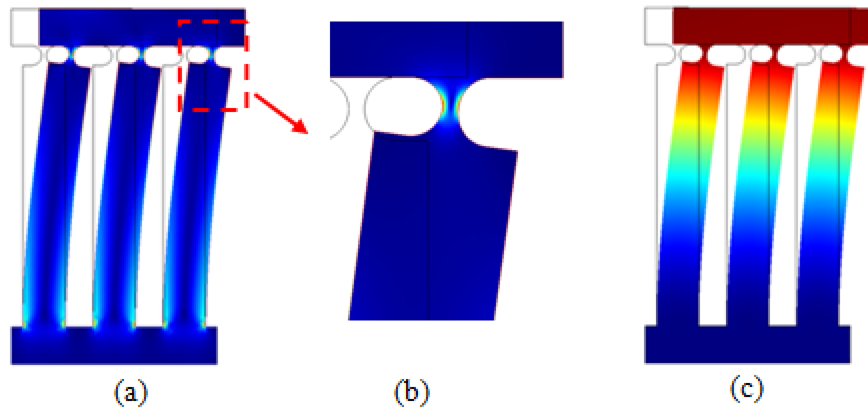

Figure 8: (a) Stress distribution and (b) Stress distribution at a flexure hinge, (c) total displacement distribution (multiplied by 40).

Moreover, the stress distribution in the hinge shows that the dominant deformation in the flexure hinge is the bending around the Z axis direction, since the maximum stresses are located on the side surfaces of the hinge. It is also shown in Figure 8(c) that the deformation of the designed mechanism agrees with the motion of parallelogram mechanisms. The displacement of the end-effector is translational motion along the x-axis with negligible parasitic rotation.

One potential disadvantage of the hybrid compliant-notch flexure over the distributed compliance-flexure is its relatively low stiffness in the Z direction, due to the additional flexure hinge structures. Even though the system is not designed to be used under heavy load, there will be some loads in Z axis from its own weight, the sample and sample holder's weight, and the force from the manufacturing processes. As part of the FEM analysis, the out-of-plane stiffness is estimated for these two flexure configurations. A load in Z-direction is applied to the end-effector of the mechanisms, and the Z-displacement and out-of-plane stiffness are estimated. From FEM analysis, the degradation of the out-of-plane stiffness of the hybrid flexure is only about 10% with a stiffness of $1.55\text{x}10^7$ N/m, compared with the distributed-compliance flexure with the Z-stiffness of $1.82\text{x}10^7$ N/m. Considering the small load in the micro/nano-manufacturing applications, such degradation of the Z-stiffness is not significant.

2.5 Application of the hybrid flexure modules

The high-bandwidth high-accuracy hybrid flexure-based nano-positioning modules can be applied to a variant of applications. A single hybrid flexure module can be used as a one degree-of-freedom nano-positioner. Such nano-positioning modules can also be configured to build a multi-degree-of-freedom nano-positioner. By directly assembling two nano-positioning modules orthogonal to each other, a XY positioning system can be built conveniently with low cost (Figure 9(a)).

Besides its direct usage in micro/nano-positioning, parallelogram flexure mechanisms are widely used as the basic building blocks for many low degree-of-freedom parallel kinematic stages, such as XY and XYZ micro/nano-positioning stages [12, 14, 15]. Figure 9(b, c) demonstrate two examples of parallel kinematic XY stage design.

In these designs, parallelogram mechanisms restrict all rotational degree-of-freedom of the end-effector, and they are the basic constituent units in these stage designs. The hybrid flexure modules can be applied as parallelogram mechanisms to achieve better structural bandwidth and positioning accuracy. Figure 9(d) shows a fabricated nano-positioning XY stage with the scheme from Figure 9(c) adopting the hybrid flexure mechanism.

In this specific design, the hybrid flexure mechanism is designed to have $T = 1.5mm$, $L = 19mm$, $t = 0.5mm$, $R = 0.5mm$, $w = 10mm$. The natural frequency of the overall device is estimated by FEM analysis and verified experimentally.

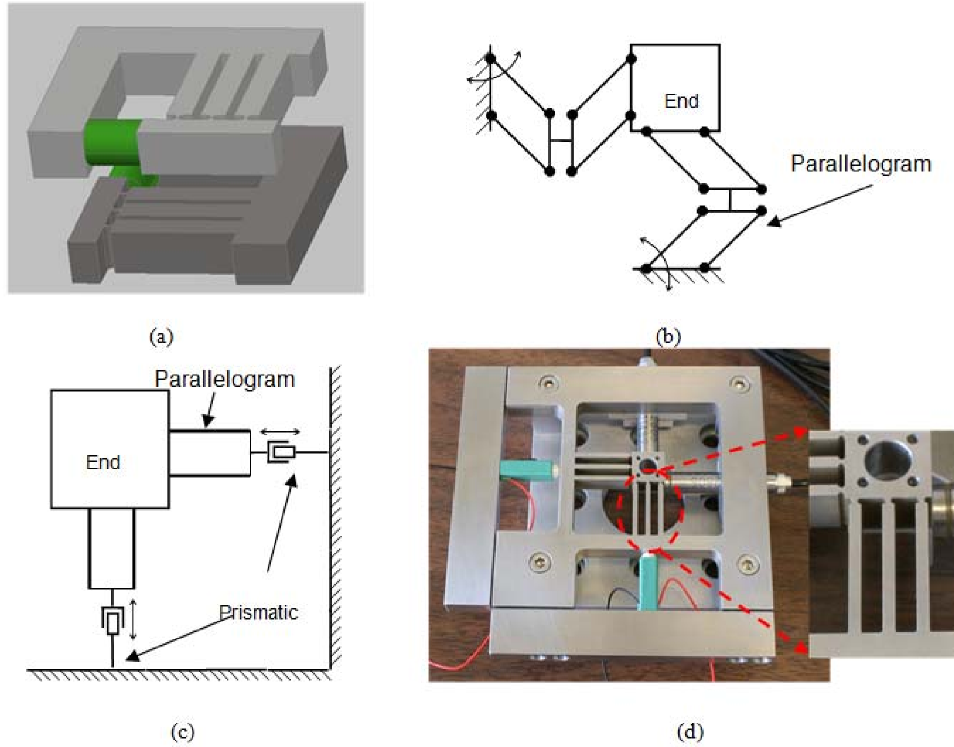

Figure 9: (a) Two dimensional (XY) micro-positioning system. (b) Scheme of parallel kinematic XY stage design using parallelogram mechanisms [15]. (c) Another XY stage design with prismatic joints and parallelogram mechanisms [28]. (d) A high bandwidth XY stage implemented from scheme (c).

A frequency test is performed on this device and the natural frequency of the device is recorded. A very high structural frequency (>8k Hz) is obtain from such XY stage design. More detailed information about this system is presented in Chapter 3, which is devoted to the design, analysis and testing of this new hybrid flexure XY mechanism.

2.6 Conclusions

This chapter introduces the design of a new single degree-of-freedom high-bandwidth high-precision hybrid compliant-notch flexure-based nano-positioning module for high-throughput nano-manufacturing applications. Compared with widely used lumped-compliance mechanisms and distributed-compliance mechanisms, the hybrid flexure module adopts a hybrid flexure structure that is composed of compliant beams and notch-flexure hinges. This hybrid flexure design decouples the performance objectives for the structural bandwidth and parasitic accuracy that are correlated in the lumped-compliance flexure and distributed-compliance flexure. The parallelogram hybrid compliant-notch flexure enables simultaneously achieving a higher structural bandwidth and a smaller parasitic motion.

The behavior of the hybrid flexure-based nano-positioning module is analyzed theoretically with respect to its design parameters and performance objectives. The results from the theoretical analysis and FEM analysis demonstrate the effectiveness of the hybrid flexure design over the widely used compliant mechanisms (lumped-compliance mechanisms and distributed-compliance mechanisms), especially when a high structural bandwidth is desired for high-throughput nano-manufacturing applications. The resulted nano-positioning modules demonstrate great flexibilities and applicability for nano-positioning applications by providing the basic building blocks for complex multi-degree-of-freedom serial kinematic and parallel kinematic micro/nano-positioning systems. The next chapter is devoted to the design, analysis and testing of a 2 DOF nano-positioning system using these modules as

building blocks, and chapter 4 presents a specific application of this new design in micro/nano-manufacturing.

The material contained in this chapter has been already accepted for publication by Journal of Manufacturing Systems, and was presented in "Proceedings of the 2009 Industrial Engineering Research Conference", Miami, Florida, June 2009 [29].

CHAPTER 3: Two degrees of freedom nano-positioning system

3.1 Introduction

Micro/nano-positioning systems with nanometer level resolution and accuracy are critically important for micro and nanotechnology. Nano-positioning stages are widely used in various applications, such as scanning probe microscope [2, 9], micro/nano-manipulation and manufacturing [3, 10, 11, 12, 13], and optical alignment [28]. The majority of the state-of-art nano-positioners utilize flexure-based structures, due to their smooth and friction-free motion and high durability without wear and deterioration. Piezoelectric actuators and high resolution displacement sensors are widely used with flexure-based mechanisms to obtain displacement with nanometer level resolution.

A high natural frequency (open-loop bandwidth) is a critical requirement for nano-positioners in high-throughput nano-manufacturing and nano-metrology applications. Most of nanoscale manipulators and manufacturing processes have extremely fast speed. For example, the micro cantilevers that are used in scanning probe microscopes [17, 18, 19, 20] and dip-pen nano-lithography [22, 23] have bandwidths over 10-100 kHz. Fast manipulation and manufacturing processes place increasingly demanding performance requirements on nano-positioning systems. The slow response speed of nano-positioners becomes a bottle neck for achieving high-rate nano-manufacturing and nano-metrology (e.g. high-speed imaging). A high-speed nano-positioning system can significantly increase the manipulation and manufacturing efficiency. High precision and high accuracy are also essential for nano-

scale manipulation and manufacturing. Closed-loop control is very important to obtain the required precision and accuracy. The achievable closed-loop bandwidth of a flexure-based nano-positioning system is generally limited by the resonant frequency of the nanopositioner due to the low damping characteristics of such flexure-based systems. A nano-positioning system with high natural frequency provides better performance capabilities for achieving a large bandwidth of the closed-loop control system.

The structural bandwidth (i.e. natural frequency) and accuracy are often contradictive performance requirements for a multiple degree-of-freedom flexure-based nano-positioner. The natural frequency of a flexure device can be improved through increasing the structural stiffness and decreasing the moving mass of the flexural structure. However, for the widely used flexure-based structures (e.g. compliant mechanisms and notch-flexure-hinges), simply scaling up the dimension of flexure components will bring severe side effect (e.g. parasitic rotary motion of the end-effector). As the stiffness of the flexure-based mechanism is increased for higher bandwidth, the parasitic motion of the system will increase as well, due to the undesired stress distribution and non-linear elastokinematic effects [25] over the mechanism when the dimension of the flexural components is scaled up. The high-bandwidth structures need to be designed carefully to minimize the parasitic motion for achieving high-bandwidth and high-accurate nano-positioners.

There are many previous efforts in developing high-speed scanners. A mechanical resonator (tuning fork) [29] were used as the scanning stage for a fast scanning axis. The provided motion from this approach is limited to mechanical vibration and incapable of precise

position control over the stage displacement. Ando and his team [30, 31] utilized stiff piezo-stack actuators to build XY positioning stages with high resonance frequency with limited motion range and operated these stages at open-loop mode. These stages were used in an atomic force microscopy to obtain real-time imaging of biomolecular processes. Schitter et. al. [32] developed a high-speed scanner based on compact flexures and actuated by piezo-stack actuators. Each axis is equipped with two actuators that are configured in a push-pull configuration. Leang et. al. [33] developed a high speed serial kinematic XY scanner for scanning probe microscope, in which the two axes are connected together in serial, in which one axis is carried by the other. As a result, one axis has a faster response than the other and the performances of the two axes are different from each other. Such configuration works better for line-by-line scanning applications in scanning probe microscopy than general purpose nano-positioning applications.

Parallel kinematic designs have been adopted in many micro/nano-positioning stages [34, 35, 36, 37, 5, 38, 39]. Compared with serial kinematic designs, parallel kinematics mechanisms can achieve a uniform performance inside the workspace. Furthermore, if appropriately designed, PKMs can result in configurations with nearly complete decoupling of the actuation effect and better positioning accuracy. Micro-positioning stages based on the parallel kinematic mechanism with different degree-of-freedom [40, 35, 36, 37, 5, 38, 39] demonstrate good performance capabilities in their motion range and resolution. However, high bandwidth is still a challenging issue for such mechanisms, since the required high

bandwidth cannot be simply obtained by scaling up the dimension of flexure components due to the requirement for high accuracy.

In this chapter, a high bandwidth XY nano-positioning system is designed and tested. The high-speed nano-positioner is expected to address applications such as high-throughput nanoscale metrology, imaging and manufacturing. The developed system is intended to achieve a high natural frequency while keeping the parasitic motion as low as possible.

A parallel kinematic mechanism is designed with two independent kinematic chains that connect the base to the end-effector in parallel. Each kinematic chain includes a prismatic joint that is actuated by a piezoelectric stack actuator and a parallelogram hybrid flexure mechanism. The parallelogram hybrid flexure mechanism is connected to the end-effector or the table. Each axis allows only planar translation with actuation in a single direction. The two kinematic chains are placed orthogonal to each other, thus spanning the XY plane. Kinematic and dynamic analyses show that the mechanical structure of the stage has decoupled motion in XY direction and has achieved high bandwidth.

Finite element analysis is adapted to verify the kinematic and dynamic responses from theoretical analysis. Two capacitive gauges were added to the system to build a closed-loop nano-positioning system. The results from frequency tests show that the resonation frequencies of the dominant vibration modes are over 8 kHz. The stage is capable of about 15 microns of motion along each axis with a resolution of about 1 nanometer. Due to the parallel kinematic mechanism design, a uniform performance is achieved across the workspace. A PI

(Proportional-Integral) controller is implemented for the stage and a closed-loop bandwidth of 2 kHz is obtained.

3.2 Mechanical design and kinematic analysis

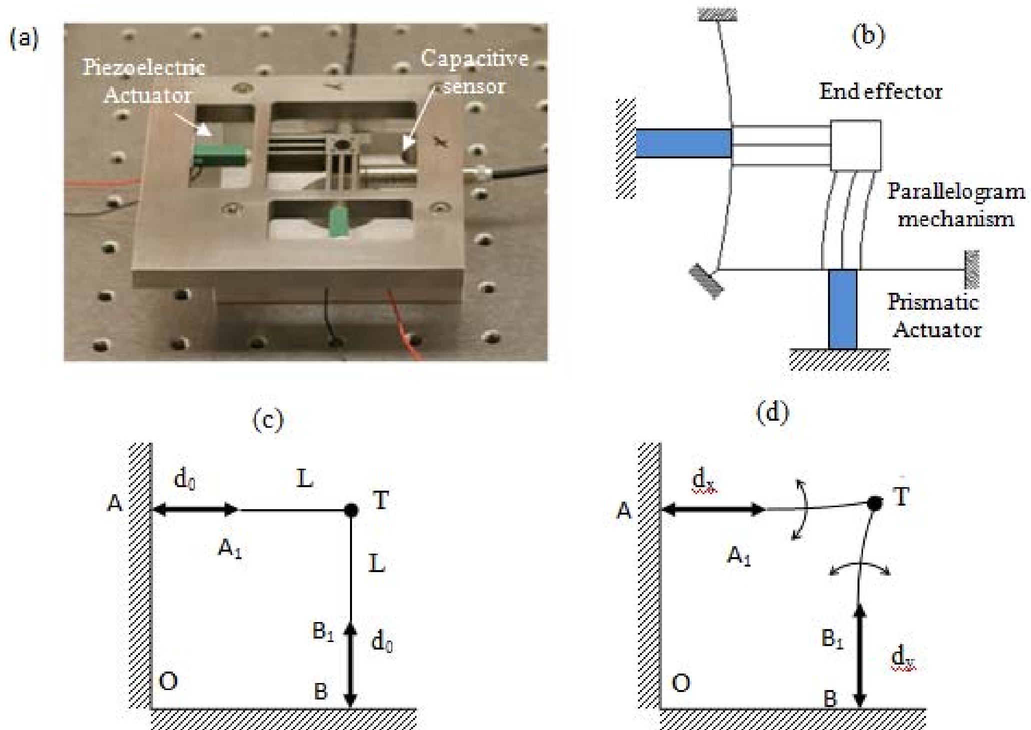

Figure 10: (a) Mechanical structure of the XY nanopositioning system (b) Schematic representation of the system (deformed system when x axis is actuated) (c, d) Equivalent linkage of the parallel kinematics XY stage for the purpose of analysis at the nominal position and under actuation.

The design of the XY stage is schematically shown in Figure 10. In this parallel kinematic design, there are two independent kinematic chains that connect the end-effector to the base. Each kinematic chain includes two serial connected joints: a prismatic joint that provides

pure translational motion and a parallelogram mechanism that provides rotary displacement while holding the orientation of the end-effector invariant. The orientation of the two chains is arranged in a way such that the prismatic joints are perpendicular to each other, kinematically decoupling the two actuated joints to the maximum extent possible. The two kinematic chains are identical to each other, which results in identical dynamics of the stage along any direction in the XY plane. Due to the symmetric configuration of the kinematic chains, the stage has the same stiffness and bandwidth in the XY plane, thus possess uniform performance in its workspace. The parallelogram mechanism restricts all rotational degree-of-freedom of the end-effector. The parallelogram compliant mechanism has equal lengths for its beams and maintains parallelism between the connector and its base. As a result, the connector undergoes pure translation along a circular path. When the stage is actuated in one direction by the prismatic joint of that chain, the resulting motion of the end-effector is accommodated by the other kinematic chain by an angular displacement at the parallelogram compliant mechanism.

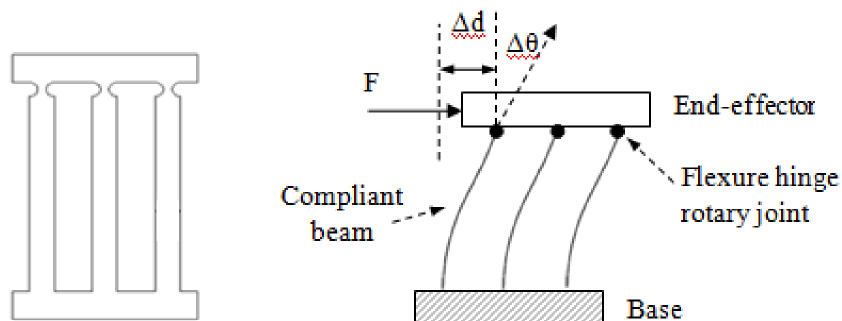

Figure 11: Illustration of the hybrid compliant-notch parallelogram flexure module.

To implement this mechanism design, the prismatic joints are replaced by doubly-clamped beams as linear guides, and they are actuated by piezoelectric actuators. The doubly-clamped beams have large compliances in the actuation direction and a very large stiffness in the lateral direction. The parallelogram mechanism is implemented by a hybrid compliant-notch flexure (Figure 11), in which each linkage includes a compliant beam and a circular flexure hinge at the end of the beam. The parallel beams provide high structural stiffness to the studied system, while the flexure hinges help to relief the undesired stress concentration at the end of the beams and make the connector orient to the base very well. Compared with widely used lumped-compliance mechanisms (using notch-flexure-hinges) and distributed-compliance mechanisms (using compliant-flexure-beams), the hybrid flexure decouples the performance requirements for the structural bandwidth and parasitic accuracy that are correlated in the lumped-compliance mechanisms and distributed-compliance mechanisms [36]. The parallelogram hybrid flexural structure enables simultaneous achievement of a higher structural bandwidth and a smaller parasitic motion.

To simplify the kinematic analysis of the mechanism, virtual links are used to represent the kinematic model. Adding a link between the base and connector of a parallelogram mechanism does not change its mobility, provided that this link has the same length as the other links and is parallel to them. Thus a virtual link is used to represent the parallelogram mechanism. The simplified kinematics model is shown in Figure 10 (c) and (d). The link AA_1 and link BB_1 represent two prismatic joints with an initial length d_0 and this length will be changed along with actuation effect. The link TA_1 and link TB_1 represent virtual links

with a fixed length L. Here the motion of point T completely represents the motion of the end-effector, because it only undergoes pure translation.

For the kinematic analysis, the relationship between actuation displacement, which is linear displacement of two prismatic joints, and the displacement of the stage, needs to be found. In Figure 10, the coordinates of point O are chosen as the origin (0, 0), then the position where the kinematics chains connected to the base are A (0, d_0+L), B (d_0+L, 0). The nominal position for the table in this coordinate system is (d_0+L, d_0+L). After the prismatic joints are actuated to d_x and d_y, the coordinates at the end of the joints are A_1 (d_x, d_0+L), B_1 (d_0+L, d_y). The coordinates of the new position of the table T now can be solved as the length of the second joints remain the same. Let the position of the stage be (x,y), under the assumption of small displacement of the parallel beam, which is validated by micro/nano-positioning applications, we have $|TB_1| = |TA_1| = L$, which satisfy the relationships given in equations 3.1 and 3.2.

$$(x - d_x)^2 + (y - d_0 - L)^2 = L^2 \tag{3.1}$$

$$\left(y - d_y\right)^2 + (x - d_0 - L)^2 = L^2 \tag{3.2}$$

Differentiating equations 3.1 and 3.2 with respect to x and y at the operation points, we get the instant relationship between the actuation displacement Δd_x and Δd_y and the displacement of the end-effector Δx and Δy through its Jacobian matrix.

$$\begin{bmatrix} \Delta d_x \\ \Delta d_y \end{bmatrix} = \begin{bmatrix} 1 & 0 \\ 0 & 1 \end{bmatrix} \begin{bmatrix} \Delta x \\ \Delta y \end{bmatrix} \tag{3.3}$$

$$\begin{bmatrix} \Delta x \\ \Delta y \end{bmatrix} = J \begin{bmatrix} \Delta d_x \\ \Delta d_y \end{bmatrix} = \begin{bmatrix} 1 & 0 \\ 0 & 1 \end{bmatrix} \begin{bmatrix} \Delta d_x \\ \Delta d_y \end{bmatrix} \tag{3.4}$$

Here,

$$J = \begin{bmatrix} \frac{\delta x}{\delta d_x} & \frac{\delta x}{\delta d_y} \\ \frac{\delta y}{\delta d_x} & \frac{\delta y}{\delta d_y} \end{bmatrix} = \begin{bmatrix} 1 & 0 \\ 0 & 1 \end{bmatrix} \tag{3.5}$$

The diagonal Jacobian matrix in equation 3.5 indicates a decoupled motion in X and Y directions around the operational point, when the device undergoes a small displacement relative to the overall dimensions of the stage (which is just the case for the nano-positioner). The effect of crosstalk between different axes (at the first order of approximation) is zero. One actuator will generate displacement in X direction and the other in the Y direction.

The actuation force from the actuator not only displaces the doubly-clamped beam and parallelogram compliant beams, but also the rotary flexure hinges at the end of the parallelogram beam. To correctly predict the total displacement and dynamic behavior of the mechanism, the relationship between the angular deflection of all the hinges and the position

of table need to be derived. As shown in Figure 11, when an actuation effect is applied to the mechanism, a displacement of *Δd* is generated at the end-effector and also at the tip of the parallel beams. Since the end-effector is parallel to the base, the flexure hinges absorb the rotary deflection of the cantilever beam, thus the rotational angle of the hinge is equal to the deflection angle at the tip of the beam. When the deflection is small compared with the overall size of the mechanism, which is the case for micro/nano-positioning, the beam deflection angle and the rotary angle of the flexure hinges is given as follows:

$$\Delta\theta \approx \frac{3}{2}\frac{\Delta d}{L} \tag{3.6}$$

When one axis is actuated by a displacement of Δd , the parallelogram compliant structure on the other axis will also be displaced by Δd to decouple the motion between the two axes. Thus, we have

$$\Delta\theta_x \approx \frac{3}{2}\frac{\Delta y}{L} \tag{3.7}$$

$$\Delta\theta_y \approx \frac{3}{2}\frac{\Delta x}{L} \tag{3.8}$$

These equations give the relationship between the displacement of the end-effector and rotation angle of flexure hinges. Since such displacements are relatively small compared to the overall dimensions of the mechanism, the relationship between the angular deflection of

the hinges in the hybrid parallelogram flexure and the displacement of the end-effector can be linearized with Jacobian matrix, J_1 and its inverse, $J_{1\text{-}inv}$.

$$\begin{bmatrix}\Delta\theta_x\\ \Delta\theta_y\end{bmatrix} = J_{1-inv}\begin{bmatrix}\Delta x\\ \Delta y\end{bmatrix} = J_{1-inv}.J\begin{bmatrix}\Delta d_x\\ \Delta d_y\end{bmatrix} \tag{3.9}$$

where

$$J_{1-inv} = \begin{bmatrix}\frac{\delta\theta_x}{\delta d_x} & \frac{\delta\theta_x}{\delta d_y}\\ \frac{\delta\theta_y}{\delta d_x} & \frac{\delta\theta_y}{\delta d_y}\end{bmatrix} \tag{3.10}$$

From differentiating Equations 3.7 and 3.8 with respect to d_x and d_y, inverse Jacobian matrix $J_{1\text{-}inv}$ is given by:

$$J_{1-inv} = \begin{bmatrix}0 & \frac{3}{2L}\\ \frac{3}{2L} & 0\end{bmatrix} \tag{3.11}$$

3.3 Structural and dynamic analysis

In each axis of the designed mechanical structure, there are three mechanical components connected together, a doubly-clamped beam that act as a linear guide, a parallelogram compliant flexure with multi-beams, and flexural hinges at the end of the beams. The

actuation force is applied in the middle of the doubly-clamped beam by piezoelectric actuators.

The overall workspace of the stage is defined by the stiffness of the mechanism and the actuation force that is applied by the piezoelectric actuator. The stiffness of the doubly-clamped beam is given by

$$K_{db} = \frac{192EI}{{L_{db}}^3} = \frac{16Ew{T_{db}}^3}{{L_{db}}^3} \tag{3.12}$$

Where I is the beam's moment of inertia calculated from $I_b = \frac{w{T_{db}}^3}{12}$, E is the Young's Modulus of the structural material (i.e. stainless steel), *w* is the device thickness (8.76 mm), T_{db} is the width of the doubly-clamped beam (5.1 mm), and L_{db} is the length of the beam (46.5 mm).

For the beams in the hybrid parallelogram flexure, since the flexure hinges absorb the rotary deflection at one end of the beams, the beams behave as free cantilever beams with a stiffness of:

$$k = \frac{Ew{T_b}^3}{4{L_b}^3} \tag{3.13}$$

where T_b is the beam width (1.68 mm), and L_b is the length of the compliant beam (19 mm). Since multiple (3) beams are used as a parallelogram structure, the overall stiffness being n=3 is as follows:

$$K_b = nk = n\frac{EwT_b{}^3}{4L_b{}^3} \tag{3.14}$$

One-dimensional circular flexure hinges are used in the stage design as rotary joints. The rotary stiffness of the hinge is given by [27],

$$k_z = \frac{T_k}{\varphi} = \frac{2ET}{9\pi}\sqrt{\frac{t^5}{R}} \tag{3.15}$$

where t is the neck thickness of the flexure hinge (0.5 mm), R is the radius of a flexure hinge at the neck (0.5 mm), and T is the height of the flexure hinge or the device thickness (8.76 mm). In the parallelogram mechanism, when the end-effector of the mechanism is actuated, all the flexure hinges undergo the same deflection, thus the rotary stiffness from the flexure hinges is $K_z = nk_z$.

When the device is actuated, the work done by the actuator is balanced by the energy stored in the hinges and the beams. From the principle of virtual work:

$$\frac{1}{2}F_x\Delta d_x + \frac{1}{2}F_y\Delta d_y = \tag{3.16}$$

$$\frac{1}{2}K_{db}(\Delta d_x)^2 + \frac{1}{2}K_{db}(\Delta d_y)^2 + \frac{1}{2}K_b(\Delta x)^2 + \frac{1}{2}K_b(\Delta y)^2 + \frac{1}{2}K_z(\Delta\theta_x)^2 + \frac{1}{2}K_z(\Delta\theta_y)^2$$

This equation can be expressed in matrix form:

$$\begin{bmatrix} F_x\Delta d_x \\ F_y\Delta d_y \end{bmatrix} = \left\{\begin{bmatrix} K_{db} & 0 \\ 0 & K_{db} \end{bmatrix} + \begin{bmatrix} K_b & 0 \\ 0 & K_b \end{bmatrix} + \begin{bmatrix} K_z & 0 \\ 0 & K_z \end{bmatrix} (J_{1-inv}.J)^2 \right\} \begin{bmatrix} \Delta d_x \\ \Delta d_y \end{bmatrix}^2 \tag{3.17}$$

where F_x and F_y are actuation force for X and Y axes. Assuming only one axis (X) is actuated, we have $F_x\Delta d_x = K_{db}\Delta d_x^{\ 2} + K_b\Delta d_x^{\ 2} + K_z\left(\frac{3}{2L}\right)^2 \Delta d_x^{\ 2}$, thus $\Delta d_x = \frac{F_x}{K_{db} + K_b + 2.25\, K_z / L^2}$. The overall stiffness of the system is given by

$$K_M = \frac{F_x}{\Delta d_x} = K_{db} + K_b + 2.25\frac{K_z}{L^2} \tag{3.18}$$

From this specific design, the total stiffness is K = 39.5E6 N/m, while the doubly-clamped beam contributes more than 95% of the total stiffness.

The maximum stress inside the compliant components (e.g. beams and flexure hinges) should always be kept within the proportional limit (yield strength) for the flexure mechanism to function properly. Such maximum stress imposes a limit on the maximum achievable displacement of the designed stage. The maximum stress inside the mechanism should be within the yield strength of the material used to avoid the plastic deformation of the

compliant beams and hinges. For a flexure hinge, the maximum bending torque that can be applied to is:

$$M_{z-max} = \frac{2\sigma_p I_{min}}{t} \tag{3.19}$$

where $I_{min} = wt^3/12$, which is the smallest moment of inertia of the flexure hinge about the rotation axis; σ_p is the stress limit. The motion range limit of a flexure hinge $\alpha_{z-\max}$ and the maximum displacement of the mechanism $\Delta d_{\max}$ corresponding to the maximum bending torque are:

$$\alpha_{z-max} = M_{z-max} C_z \tag{3.20}$$

$$\Delta d_{max-z} = \frac{2}{3}\alpha_{z-max} L \tag{3.21}$$

For the parallel cantilever beam, the maximum stress occurs at the fixed end with the maximum stress to be $\sigma_{max} = \sigma_p = \frac{6FL_b}{wT_b{}^2}$. The maximum displacement that the beam undergoes before failure is:

$$\Delta d_{max-b} = \frac{2\sigma_{max} L_b{}^2}{3ET} \tag{3.22}$$

For the double-clamped beam, the maximum stress occurs at the fixed end and the middle of the beam with the maximum stress to be $\sigma_{max} = \sigma_p = \frac{3FL_{db}}{4wT_{db}^2}$. The maximum displacement that the beam undergoes before failure is:

$$\Delta d_{max-db} = \frac{\sigma_{max} L_{db}^2}{12ET_{db}} \tag{3.23}$$

The maximum achievable displacement of the device is defined by $\min(\Delta d_{\max-z}, \Delta d_{\max-b}, \Delta d_{\max-db})$. For this specific design, stainless steel is used to fabricate the nano-positioning stage. The rotation limit of the rotary hinge is $\alpha_{z-max} = \pm 0.0029\ radians$, which indicates a maximum motion range of 36 microns. The maximum motion from the parallel cantilever beams and double-clamped beams are 171 microns and 51 microns respectively. It is clear that the maximum stress concentration is located in the flexure hinges, and that the maximum displacement is bounded by their behavior.

Since compliant flexural springs are used in the structure, the device has negligible friction and hence almost no damping. As an undamped multiple-degree-of-freedom system, Lagrange's Equations are used to calculate both the vibration modes and natural frequencies. Lagrange's equation (equation 3.24) states that the variation of the kinetic energy and potential energy plus the line integral of the virtual work done by non-conservative forces during any time interval t_1 to t_2 must be equal to *0*.

$$\frac{d}{dt}\left(\frac{\partial T}{\partial \dot{q}_i}\right) - \frac{\partial T}{\partial q_i} + \frac{\partial V}{\partial q_i} = Q_i, \qquad i = 1,2,\ldots N \tag{3.24}$$

where, T represents the total kinetic energy of the system, V is the potential energy which includes both strain energy and the potential of any conservative external forces, where q_i represent linearly independent generalized coordinates, Q_i represents generalized non-conservative forces, and N is the number of generalized coordinates, which is also equal to the number of DOF of a system (two for this designed stage). Assuming the hinges as perfect springs, and without considering any non-conservative forces, a multiple degree-of-freedom harmonic oscillator is expected. The stage has 2 generalized coordinates which we will conveniently use as the axes directions x and y of the table (that undergoes no rotations). For free vibrations of the stage, since there are no external or dissipative forces, $Q_i = 0$. From the kinematics of the stage, it is given that $\Delta p = J\Delta q$ where, $\Delta p = [\Delta x, \Delta y]^T$ and $\Delta q = [\Delta d_x, \Delta d_y]^T$.

The kinetic energy in the system is the summation of the energy of the double-clamped beams, parallelogram flexure beams and the end-effector. Although these beams experience both translational motion and rotation, utilizing the effective mass, the structural dynamic analysis can be simplified by assuming such cantilever beams undergoes pure translation with the effective mass. The effective mass of the parallelogram linkage and double-clamped beams can be expressed by $m_b = c \times M_b$, and $m_{db} = c \times M_{db}$ where c is the coefficient of the

effective mass with a numerical value 33/140 from [36]. The total kinetic energy in the system is given by:

$$T = T_{db} + T_b + T_E = \frac{1}{2}[v_x \quad v_y] M \begin{bmatrix} v_x \\ v_y \end{bmatrix} = \frac{1}{2}[v_x \quad v_y] \begin{bmatrix} M_x & 0 \\ 0 & M_y \end{bmatrix} \begin{bmatrix} v_x \\ v_y \end{bmatrix} \tag{3.25}$$

where $v_x = \Delta \dot{x},\ v_y = \Delta \dot{y}$

Here M is the mass distribution matrix with

$$M_x = m_{db,x} + M_{b,x} + m_{b,y} + M_e = cM_{db} + (1+c)M_b + M_e \tag{3.26}$$

and

$$M_y = m_{db,y} + M_{b,y} + m_{b,x} + M_e = cM_{db} + (1+c)M_b + M_e \tag{3.27}$$

The potential energy in the system is given by the energy stored as elastic deformation of the hinges and compliant beams. The strain energy of a flexure hinge deformed by an angle of $\Delta\theta$ is $V = \frac{1}{2}k\Delta\theta^2$, and in a compliant beam deformed by a displacement Δd is $V = \frac{1}{2}k\Delta d^2$.

Here k is the stiffness of the flexure hinge and compliant beam. For this mechanism, the energy stored in the double-clamped beam when the table has moved by $\Delta p = [\Delta x, \Delta y]$ is given by:

$$V_{db} = \frac{1}{2} K_{db} [\Delta d_x \quad \Delta d_y] . \begin{bmatrix} \Delta d_x \\ \Delta d_y \end{bmatrix} = \frac{1}{2} K_{db} [\Delta x \quad \Delta y] . [J^{-1T} \quad J^{-1}] \begin{bmatrix} \Delta x \\ \Delta y \end{bmatrix} \tag{3.28}$$

The energy stored in the parallelogram beams when the table has moved by $\Delta p = [\Delta x, \Delta y]$ is given by:

$$V_b = \frac{1}{2} K_b [\Delta x \quad \Delta y] . \begin{bmatrix} \Delta x \\ \Delta y \end{bmatrix} \tag{3.29}$$

and the energy stored in the flexural hinges is:

$$V_z = \frac{1}{2} K_z [\Delta \theta_x \quad \Delta \theta_y] . \begin{bmatrix} \Delta \theta_x \\ \Delta \theta_y \end{bmatrix} = \frac{1}{2} K_z [\Delta x \quad \Delta y] . [J^{-1T} \quad J^{-1}] . \begin{bmatrix} \Delta x \\ \Delta y \end{bmatrix} \tag{3.30}$$

Therefore the total potential energy in the system is given by:

$$V = V_{db} + V_b + V_z = \frac{1}{2} [\Delta x \quad \Delta y] . [K_{db} J^{-1T} J^{-1} + K_z J^{-1T} J^{-1} + K_b I] . \begin{bmatrix} \Delta x \\ \Delta y \end{bmatrix} \tag{3.31}$$

Differentiating equations 3.25 and 3.31 and inserting them into equation 3.24, the dynamics equation from the stage is given as:

$$\begin{bmatrix} M_x & 0 \\ 0 & M_y \end{bmatrix} \begin{bmatrix} \Delta\ddot{x} \\ \Delta\ddot{y} \end{bmatrix} + [K_{db}J^{-1T}J^{-1} + K_z J^{-1T}J^{-1} + K_b I].\begin{bmatrix} \Delta x \\ \Delta y \end{bmatrix} = 0 \ or \tag{3.32}$$

$$\begin{bmatrix} M_x & 0 \\ 0 & M_y \end{bmatrix} \begin{bmatrix} \Delta\ddot{x} \\ \Delta\ddot{y} \end{bmatrix} + K.\begin{bmatrix} \Delta x \\ \Delta y \end{bmatrix} = 0$$

Thus, it is a 2-DOF harmonic oscillator. The eigenvectors of $M^{-1}K$ will give the modal directions for the system and the corresponding eigenvalues λ_i, give the corresponding modal frequencies $f_i = \frac{1}{2\pi}\sqrt{\lambda_i}$. Based on the design of the compliant flexural components and the numerical values for the different matrices, the modal directions along X and Y directions and a main resonant frequency of 7130 Hz are found.

3.4 Design Considerations for a high-bandwidth stage

The kinematic scheme presented in the previous section had to be adapted for physical realization of a flexure-based, parallel kinematic nano-positioning stage. The monolithic stage structure that includes a doubly-clamped beam and a parallelogram hybrid flexure module for each axis is fabricated on a wire-EDM (Electrical Discharge Machining) machine. To achieve a high-bandwidth, the mechanical structure needs to have a large stiffness and large natural frequency. Besides the required high overall mechanical stiffness, the stiffness needs to be distributed to different compliant components properly to achieve the performance requirements on bandwidth and accuracy. The kinematic analysis assumes that the doubly-clamped beam is a linear guide and provides linear displacement. However, this assumption is valid when the stiffness of the doubly-clamped beam is much larger than the stiffness

of the parallelogram flexure mechanism. Otherwise the parallelogram flexure mechanisms that connect the end-effector to the two doubly-clamped beams cannot completely decouple the behavior between the two kinematic chains. As results, the doubly-clamped beams are designed to have a large stiffness while the parallelogram flexure mechanisms are designed to have a large compliance to decouple the two axes displacements. On the other hand, the parallelogram flexure mechanisms still need to have a minimum stiffness to support the end-effector and make sure the local vibration modes will not deteriorate the overall natural frequency of the device.

Piezoelectric actuators were chosen because of their high bandwidth, high resolution and simple structure. The actuation direction is normal to the doubly-clamped beam that the actuator is attached to as shown in Figure 10 (a). To achieve a desired displacement range of 15x15 microns, two piezoelectric actuators (blocking force of 1600 N, maximum displacement of 28 μm, maximum voltage of 150 V) were chosen for this stage to provide the actuation forces for the two axes. The actuator has an unloaded resonant frequency of 50 kHz and a capacitance of 1800 nF. The piezoelectric actuators are assembled in-between the doubly-clamped beam and the base by preloading the doubly-clamped beam. The restoring force holds the actuator in position and provides the preload force for the actuator. The electrical components of the nano-positioning system also limit the maximum achievable bandwidth of the system. Due to the capacitance of the piezoelectric actuator, it takes time for the piezo-amplifier to fully charge the capacitor to reach the desired actuation voltage. Large current and high power is generally required for the piezo-amplifier to achieve a high operation speed and large bandwidth of the overall system. Piezo-amplifiers with the

maximum current of 1A and output voltage of -30V to 150V are selected to drive the actuator.

Capacitive sensors (Probe 2805 and Gauging Module 8810 by ADE Technologies, range +/- 5μm, bandwidth 10 kHz with analog output of +/-10 V) are used as displacement sensors to directly sense the motion of the end-effector. The targets for the capacitive sensors are provided by a cubical metal block with two polished orthogonal surfaces, mounted on to the bottom of the end-effector. The sensors are fixed to the base to measure displacement by sensing the change in capacitance due to the motion of a metal target block on the end-effector. As non-contact sensors, they do not contribute to load, friction or wear. Further, the setup and calibration are relatively easy and the resolution obtained is significantly higher than most other types of displacement sensors.

The stage assembly is constructed by mounting the target block, capacitive probes and piezoelectric actuators on to the monolithic flexure structure. The assembled device is shown Figure 10 (a).

The final dimensions of the different parts depend on the specific applications. Keeping the characteristics explained in this section, the stiffness of the system can be adjusted as desired considering also the achievable working space (maximum displacement). A pre-design of the system is achieved through theoretical analysis, while the final dimensions are set after verifying the system's behavior using FEM analysis. Then, the piezoelectric actuator

maximum force must also be considered to guarantee that it is capable of providing the required actuation force for the specific designed system.

3.5 Finite Elements Analysis and Results

In this section, FEM (Finite Element Method) analysis is performed to verify the design objectives of this high-bandwidth XY nano-positioning system. The FEM simulation is performed using COMSOL software. The global stiffness, required actuation force, and the maximum achievable displacement of the system, as well as its stress distribution are studied using static analysis. Then, the dynamic behavior of the device, such as vibration modes and their corresponding resonant frequencies are obtained from the dynamic analysis. The finite element model of the designed mechanism has the same boundary conditions to the actual assembly where all the unmovable parts are full constrained. The actuation force is applied to the middle points of the double-clamped beam. The material of the mechanism is set to be stainless steel with Young's modulus E = 205 GPa and Poisson's ratio = 0.28.

The static analysis is performed by applying the desired punctual load to the middle of the doubly-clamped beam and observes the displacement and stress of the stage. The stiffness of the mechanism and the linearity of the displacement can be estimated in this way. Figure 12 provides the relationship between the actuation force and the corresponding displacement of the end-effector from the FEA.

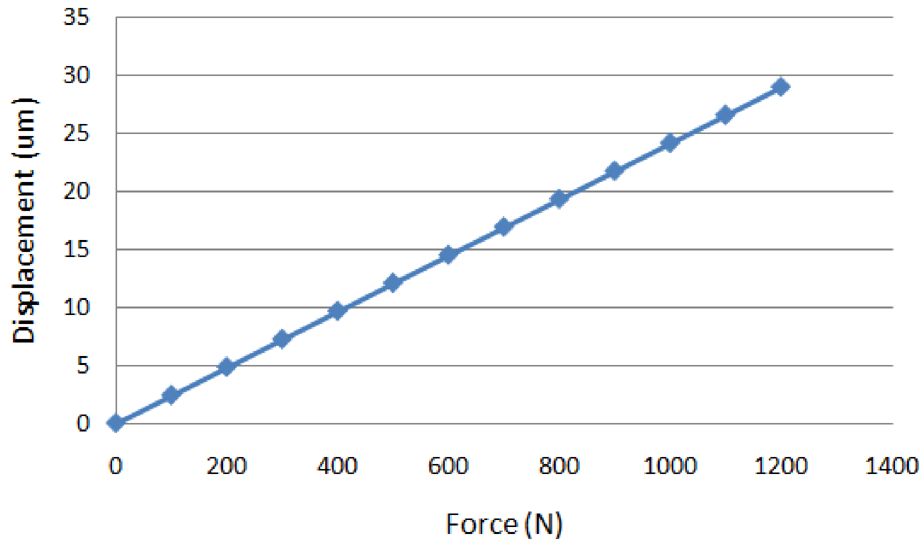

Figure 12: Stage displacement under different actuation force.

The results fit into a line very well, which indicates the good linearity of the stage response. The slope of the fitted line (i.e. stiffness of the mechanism) is 4.13 E7 N/m, which is close to the theoretic analysis.

When the actuation force is applied to the mechanism, it can be observed from the stress distribution diagram that the two ends and the middle of the doubly-clamped beam as well as the flexure hinges have the highest stress concentration (Figure 13).

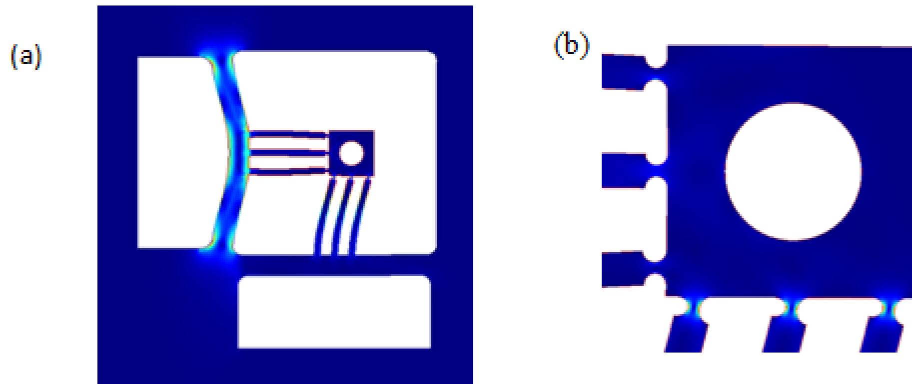

Figure 13: (a) Stress distribution of the deformed mechanism with deformation magnified by 100. (b) Stress distribution around the flexure hinges.

The actuation effect and the corresponding displacement of the mechanism need to be inside the elastic operating range such that the maximum stress of the structure is below the yield stress of the material. From the finite element analysis, a maximum actuation force of 1500 N and a maximum displacement of 36.3 μm can be obtained from the stage. These results validate the theoretical mechanical analysis in the section 3.2 and 3.3. The parasitic Abbe/sine error is evaluated by measuring the orientation of the connector, which ideally can carry translational motion in XY direction. When the axis is actuated with the maximum actuation force and the largest displacement, the parasitic orientation error is as small as 3E-3 degrees. This small parasitic error comes from the mechanism design in which the compliant parallelogram hybrid flexure mechanisms decouple the crosstalk between the two axes.

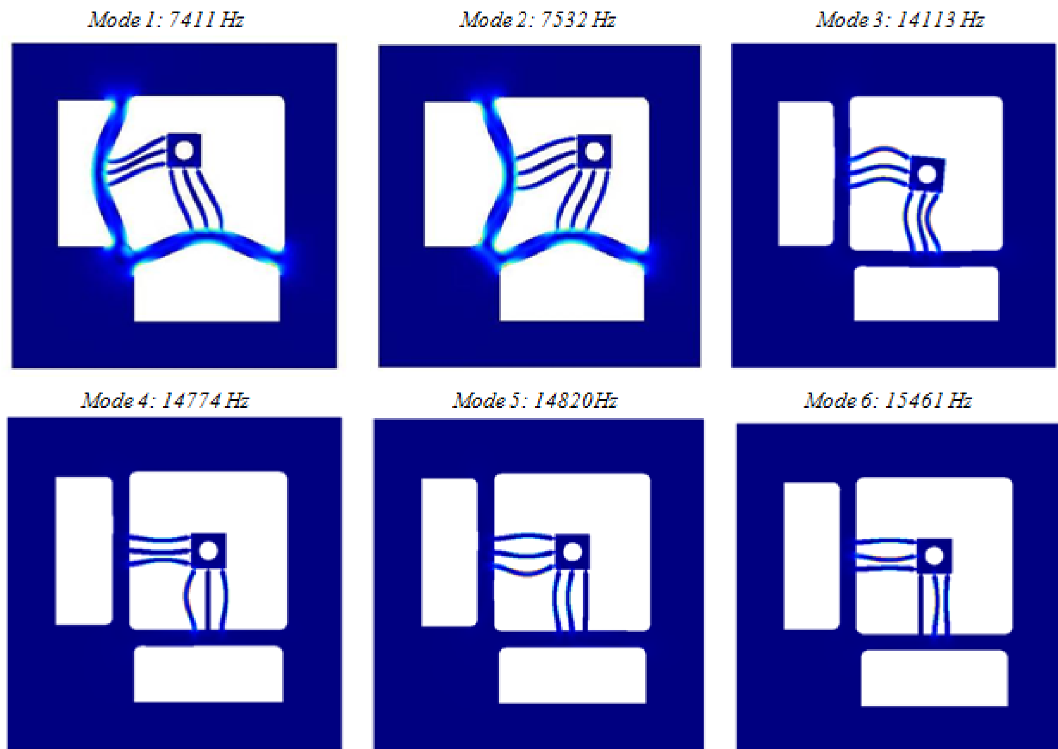

Figure 14: Vibration modes and their corresponding frequencies.

The vibration modes and corresponding natural frequencies of the stage are also analyzed by FEA. Figure 14 shows the six most dominant mode shapes for the system. Among these modes, the first two modes are related to the displacement of the end effector that is generated from the actuation effect. These two modes are the translational modes, which correspond to the in-phase and out-of-phase displacements of the two actuators and result in a displacement of the end-effector in two perpendicular directions. The modal frequencies are slightly different because of the small differences in the end-effector displacements that

occur when the parallelogram hybrid flexures bend in the same directions or in different directions.

The other four modes are related to the lateral dynamics of the parallelogram hybrid flexure mechanisms, and they are not directly related to the actuation behavior. These local vibration modes correspond to a mode that is roughly 6 times stiffer than those associated with the desired XY motions. This is attributed to the parallel kinematics XY stage design which besides producing a relatively high natural frequency associated with the dominant modal directions (the desired translational DOF in XY plane), also provides for large separation between the modes associated with the desired motion and other high-order modes. The dominant model has a resonant frequency of 7411 Hz, which verify the theoretical analysis, and provide high potential for fast operation and high-throughput.

Even though micro/nano-manufacturing applications are not associated with heavy load, there will be some loads in Z axis from the sample and sample holder's weight and the force from the manufacturing processes. The structure is desired to have a large stiffness in Z-direction and small out-of-plane motion. As part of the FEM analysis, the out-of-plane stiffness is estimated by applying a load in Z-direction to the end-effector of the mechanisms, and recording its Z-displacement.

An out-of-plane stiffness of 3.62 MN/m is obtained for the system. Considering the small load in the micro/nano-manufacturing application, the system has enough Z-stiffness to

withstand the manufacturing process without producing considerable displacements in this direction.

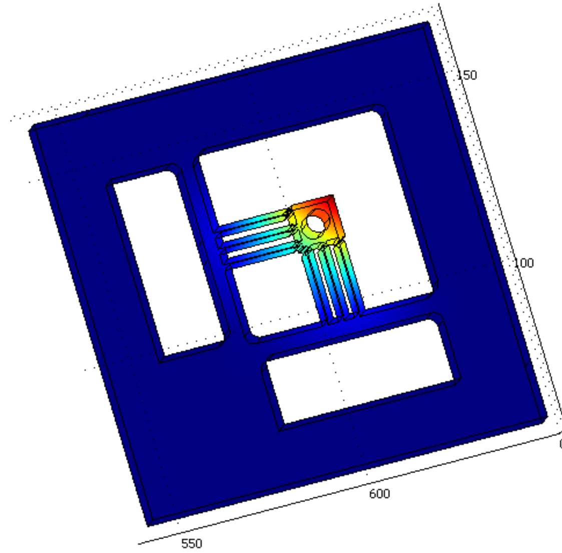

Figure 15: Out of plane displacement under Z load.

3.6 Experimental results

The fabricated device was evaluated in its static and dynamic behavior, and compared with the theoretical and FEA results. The steady state displacement of the stage under different driving voltage is shown in Figure 16. The actuation voltage is given to one axis (X), and the displacements from both axes are recorded. An almost linear relationship is obtained between actuation voltage and displacement of the actuated axis. A total displacement of 12 microns is achieved for the stage. The cross-coupling effects are negligible. When one axis (X) is fully actuated, the cross-coupling motion is only 0.2% from the other axis (Y). Such small

cross-coupling comes from the mechanism design that decouples the motion in the X and Y directions.

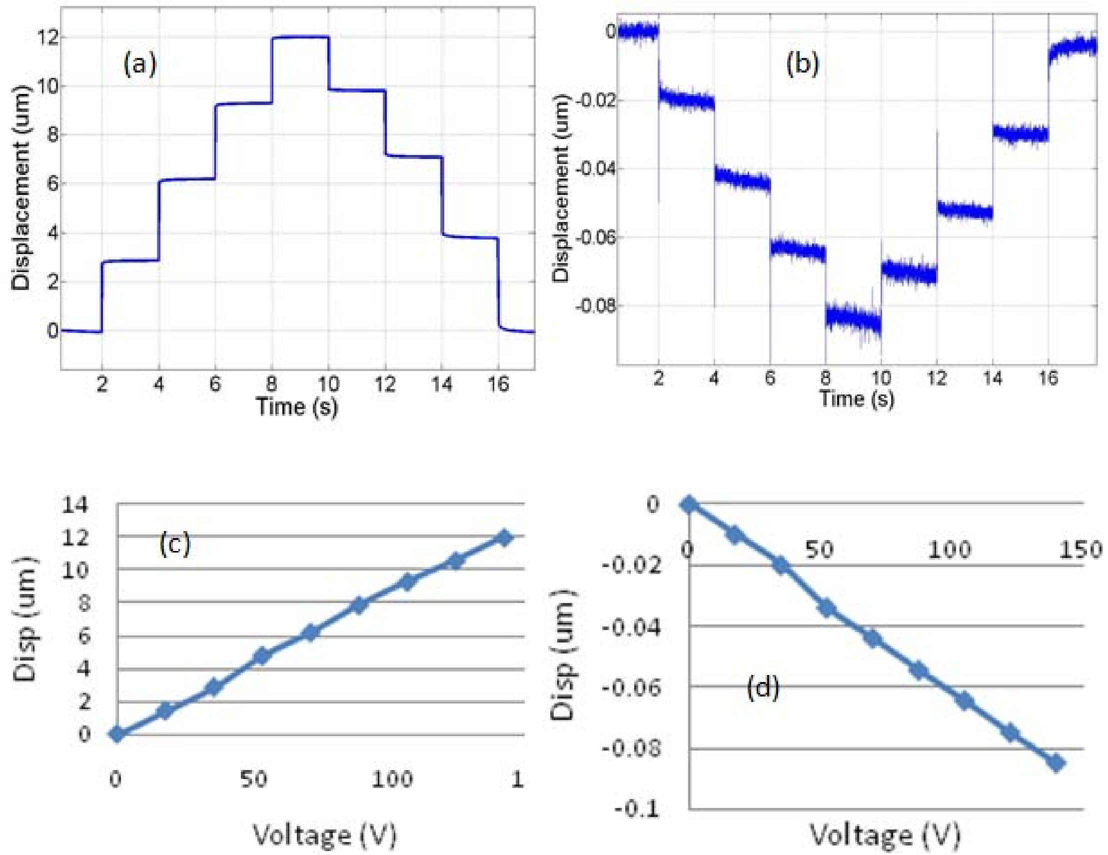

Figure 16: (a, c) Experimentally measured static displacement with respect to actuation voltage for one axis. (b, d) Cross-coupled displacement from the other axis.

The positioning error from the cross-coupling can be easily compensated by a closed-loop controller. The performance (displacement and cross-coupling) is almost identical when Y axis is actuated due to the symmetrical design of the mechanism. In the experiments results,

the hysteresis from the piezoelectric actuators can be observed from the open-loop step response from Figure 16 (a, b)). The total workspace of the stage is about 15x15microns in the XY directions.

Resolution is an important performance for a nano-positioning system. In this flexure-based system, reference signals in XY directions are directly controlled, there is no error from kinematic interpolation. The resolution is primarily restricted by noise. Due to the low damping of the mechanical structure, this high frequency noise will vibrate the stage and deteriorate the positioning resolution.

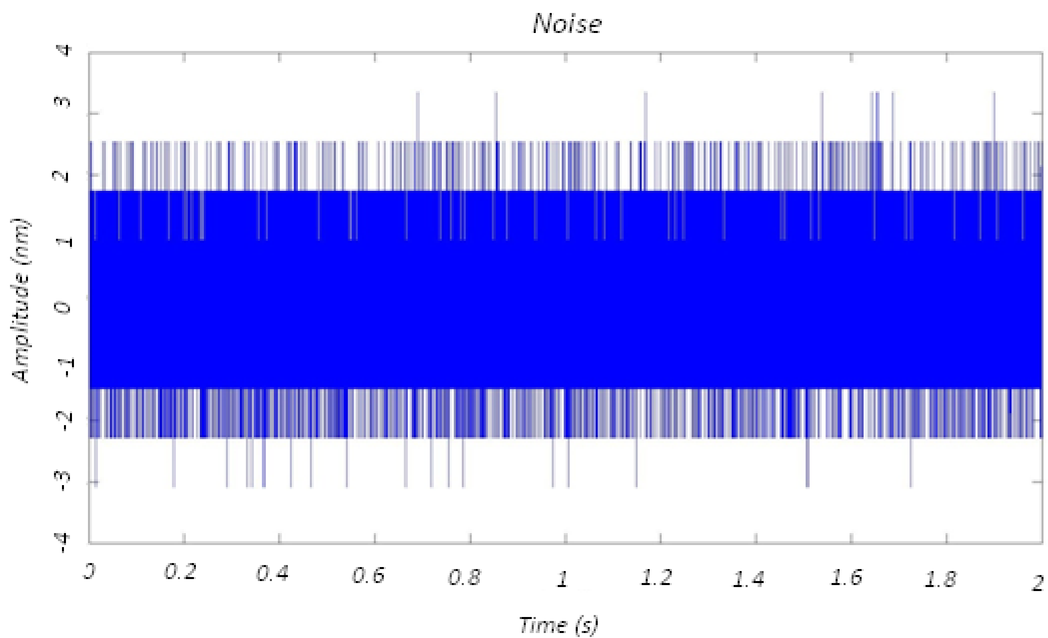

Figure 17: Steady state noise level.

Considering the sensor's accuracy as the best possible resolution of the system, the achievable resolution is limited by many other factors, such as environmental disturbance and electronic noise.

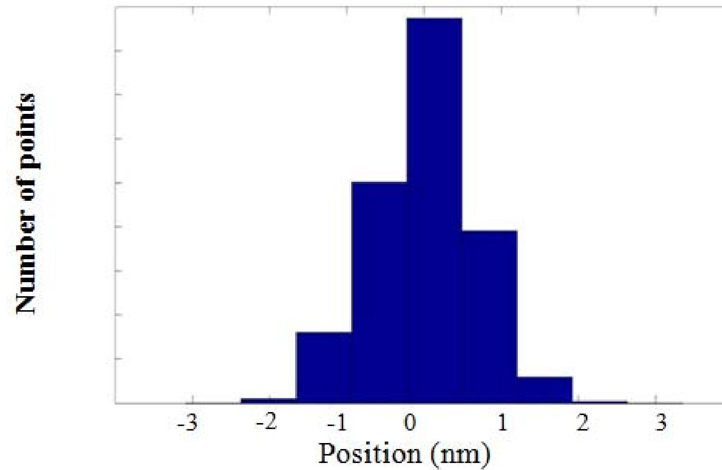

Figure 18: Noise histogram of steady state sensor measurements.

For this particular system, Figure 18 demonstrates a noise histogram of the steady state output from the position sensors. The standard deviation of the output signal is 0.77 nm when the system is actuated and hold at a command position, which indicates a nanometer level resolution.

The frequency response results were obtained by using a dynamic signal analyzer through swept-sine analysis with frequencies spanning a range of 50 kHz. The resulting frequency responses are shown in Figure 19.

The two axes have similar dynamic response with the dominant resonant peak at around 8.9 kHz. This experimental value is larger than the results from the theoretic analysis and finite element analysis. These discrepancies can be explained by approximations made in the effective mass in the system, and dimensional errors during manufacturing.

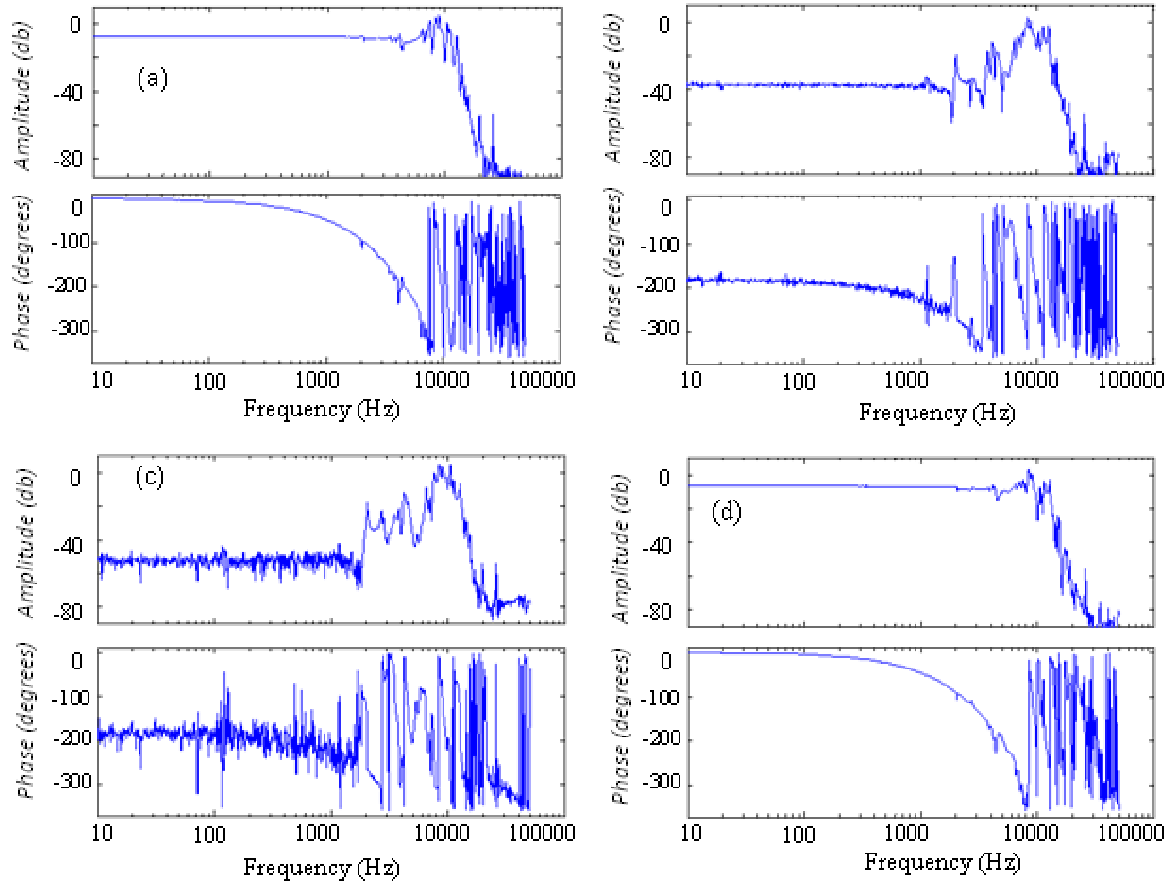

Figure 19: Frequency response of the nanopositioner. (a) From X actuator to X displacement. (b) X actuator to Y displacement. (c) Y actuator to X displacement. (d) Y actuator to Y displacement.

The stage has an almost flat magnitude response up to 6 kHz in the directly actuated axes, which provide better potential for closed-loop control design. The cross-talks between the two axes (Y-X and X-Y response) are insignificant at most of the frequency range. The DC gain of the off-diagonal response differs from the gain of the diagonal frequency response by 30 to 40db. Such cross-coupling effect can be compensated by the closed-loop control.

To construct a closed-loop system, A DSP (digital signal processing) based motion controller is used to receive displacement feedback from capacitive sensors, calculate the control out and send it to the amplifier. A high resolution (16 bits) A/D converter is used to translate the analog voltage positional signal to digital signals used by the controller.

Since the sensitivity of the capacitance sensor is 2.5μm/volt and the maximum value of the 16 bit digital signal is 10 volts, the resolution from the ADC is about 0.76 nm, which is the best resolution of the control loop. A piezo amplifier with a magnification factor of 20 is used to receive command signals from the controller and provide amplified voltage to drive the piezoelectric actuators. To close the position loop, a PI (Proportional-Integral) controller was implemented on the controller. The PI controller can obtain a larger than 1 kHz closed-loop bandwidth. Figure 20 shows the closed-loop step response of two axes.

The rising time (time between 10% and 90% of one step) for X-axis is only 180 μs with a 5% overshoot, which roughly indicates a closed-loop bandwidth of 2 kHz. Y axis has a 180 μs rising time with a 6.8% overshoot.

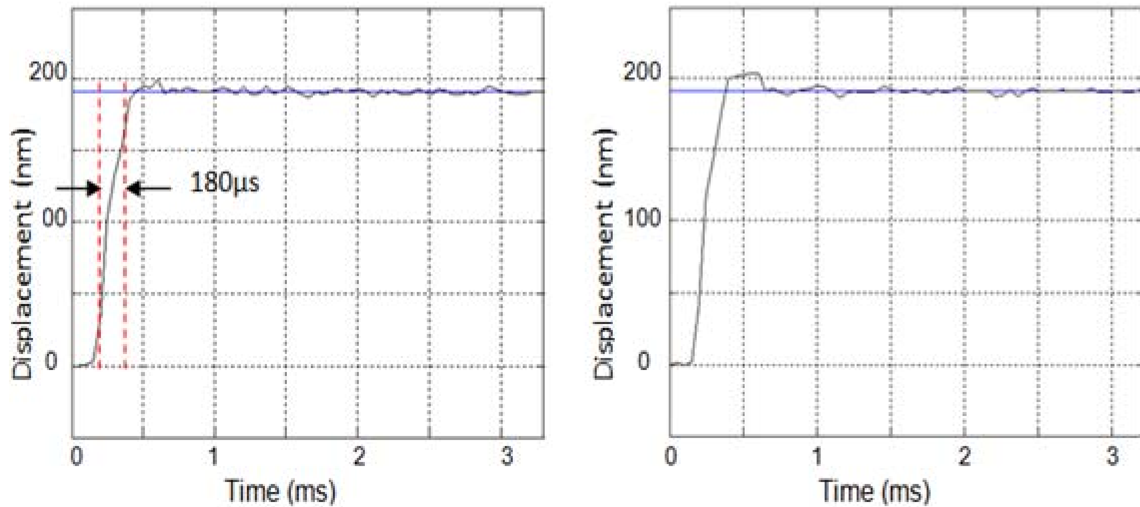

Figure 20: Closed-loop step response in X (left) and Y (right) directions.

With a mechanical design with higher resonant frequency, even a simple PI controller can gain a very high-closed loop bandwidth. Figure 21 shows the control result for stepwise motion of the stage using the PI controller. The step size was 1 µm.

Clearly, the closed-loop control provides a linear and repeatable motion, compared with open-loop operation as shown in Figure 16 (a,b), in which the nonlinear hysteresis effect from the piezoelectric actuators can be easily observed.

The steady state RMS error was less than 1nm. Figure 22 demonstrates the noise histogram of the closed-loop steady state output from the position sensors. The standard deviation of the output signal is 0.7 nm when the system is commanded at a fixed position.

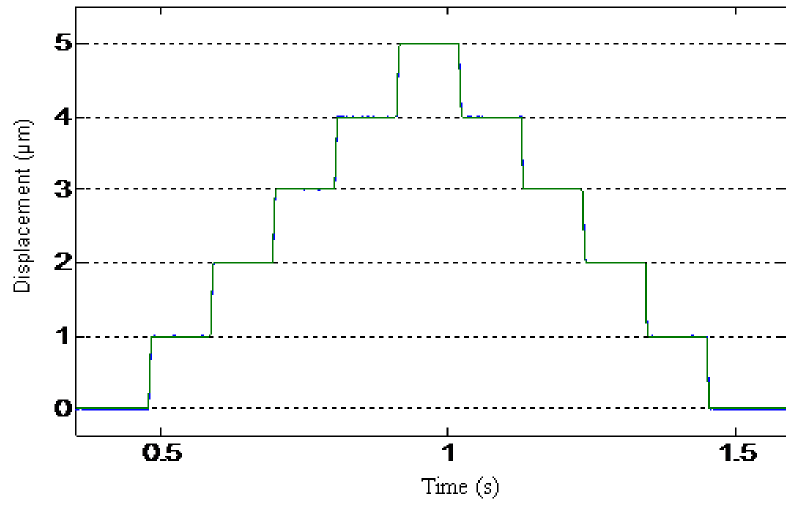

Figure 21: Closed-loop stepwise motion.

This resolution is comparable to the open-loop result, and a nanometer level control resolution is obtained for high precision and high accuracy applications.

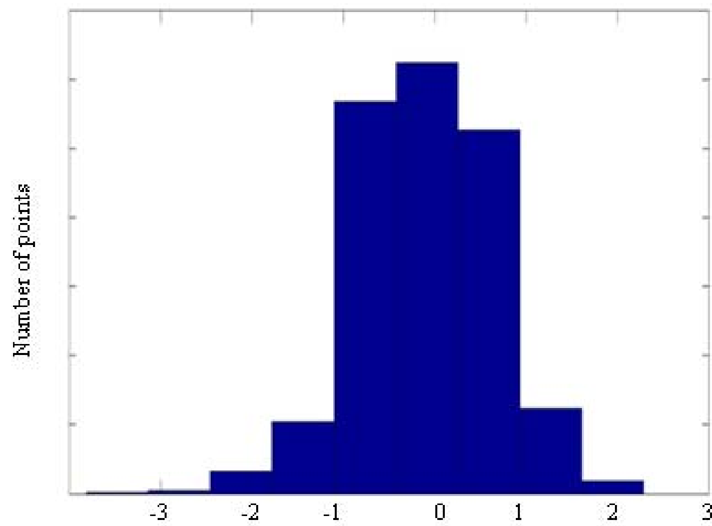

Figure 22: Histogram of closed-loop steady state error

3.7 Conclusions

In this chapter, a high-bandwidth piezo-driven parallel-kinematic nano-positioning stage is developed which can provide high-speed accurate positioning in XY plane. The design, analysis, fabrication and experimental testing are presented. The monolithic stage design has two axes and each axis is comprised of a doubly-clamped beam and a parallelogram hybrid flexure module with complaint beams and circular flexure hinges. The doubly-clamped beam that is actuated by a piezoelectric actuator acts as a linear prismatic axis. The parallelogram hybrid flexure modules are used to decouple the actuation effect from the other axis. The mechanism design decouples the motion in the X and Y directions and restricts parasitic rotations in the XY plane while allowing for an increased bandwidth with linear kinematics in the operating region (or workspace). Kinematic and dynamic analyses show that the mechanical structure of the stage has decoupled motion in XY direction, while achieving high bandwidth and good linearity. Finite element analysis is adapted to verify the dynamic responses from theoretical analysis. The stage is actuated by piezoelectric stack actuators and two capacitive gauges are added to the system to build a closed-loop positioning system. The results from the frequency test show that the resonation frequencies of the two main vibration modes are over 8 kHz. The stage is capable of about 15 microns of motion along each axis with a resolution of about 1 nanometer. Due to the parallel kinematic mechanism design, a uniform performance is achieved across the workspace. A PI controller is implemented for the stage and a closed-loop bandwidth of 2 kHz is obtained. The high-speed nano-positioner

is expected to address applications such as high-throughput nanoscale metrology, imaging and manufacturing.

The material contained in this chapter has been reviewed by Transactions of Mechatronics technical editor and resubmitted for final publication.

CHAPTER 4: Micro-milling using the designed hybrid two DOF nano-positioning stage

4.1 Introduction

Micro-manufacturing is one of the most important and active fields of study due to its broad applications in the modern industry. Gyroscopes and accelerometer for aerospace and automotive industries, biosensors and micro-needles for medical and biomedical companies, solar cells and data storages for telecommunications and information peripherals, and chemical and bio-sensors for environmental monitoring are just a few examples of the many applications that micro-manufacturing has in modern industry.

Micro-manufacturing was originated from microelectronics industry, and currently it has extended to as many and diverse applications as semiconductor manufacturing, MEMS (micro-electro-mechanical systems), nanotechnology, and biomedical applications, among others. There are many micro-manufacturing techniques that are required for these industries, such as lithography, additive processes (deposition, doping and oxidation), subtractive processes (dry and wet etching) and surface micro-machining (bulk and patterning).

There are several types of micro-machining processes that are currently applied in industry according to [41]. Removal by mechanical force, by melting and vaporization, by ablation, by dissolution, plastic deformation, solidification, lamination and recomposition are all processes that can be grouped as micro-machining. Among them, the most popular is the removal by mechanical force. It is based in the concept of removing the useless part of the work piece using mechanical force to produce plastic or brittle breakage. Different processes

such as cutting, sandblasting, ultrasonic machining and grinding can be listed as part of this group. From this group, cutting is the one that presents the best geometric correlation between the tool path and the desired features in the machined surface due to the fact that in this process, there is physical contact between a single point of the tool and the work piece.

Many alternatives have been proposed to improve these micro cutting processes. The main objectives are to decrease the size of the smallest achievable feature that can be machined, as well as better surface finish, good accuracy and high efficiency to reduce costs. The first approach that can be found in the literature is the miniaturization of the conventional scale milling process. This approach is limited by the minimum size of the micro-milling tool, especially due to the brittle characteristics of the required materials, and the extremely fast required spindle speed. Features of around 50 um in size have been achieved using hard metals micro-milling tools in brass and stainless steel [42]. Micro-milling machines with multiple degrees of freedom have also been presented as an alternative for milling miniaturization [43]. Attempts to measure and optimize the required parameters to obtain the desired surface finish and accuracy have been previously developed as shown in [44, 45].

As a second approach to reduce the minimum achievable feature size, the use of diamond or tungsten tips to create grooves over the work piece has been proposed. Atomic Force Microscopes (AFM) have been used with modified diamond tips to perform this approach using silicon work pieces achieving features as small as 5 um width [46]. Some work over metal samples has also been attempted in the past with good result and features of around 1 um [4]. A combination of these approaches was proposed in [47], using profiled tools and a

CNC cutting machine that generates a circular path to rotate the tool instead of the spindle, and also generate the required displacements to create the desired features. However, these alternatives have some problems.

In the first case, the tool size and spindle speed are the limitations. For the second approach, due to the fact that it is based on the scratching of the surface, and not on the continuous cutting that is characteristic in conventional scale machining, they present issues related to surface quality and tool life prediction. The achievable feature shapes are also limited in this approach due to the one directional nature of the process, which lack of the flexibility that conventional methods present in feature shapes. The productivity and effectiveness of the last proposed alternative [47] is limited mainly for the achievable speed in the circular path tool displacement.

In this chapter, a new micro-cutting approach is presented that is capable of producing features in the order of a few microns to several nanometers, with low cost and good accuracy. This new approach is a specific application for the previously designed two degrees of freedom nano-positioning system presented in chapter 3. This nano-positioning system provides the required tool-sample relative circular continuous displacement with an angular speed that can be of up to 360.000 rpm (6 kHz). This displacement is used instead of the traditional and limited rotary spindle to generate the tool-sample circular displacement, and in combination with a tungsten probe tip, a 1 tooth cutting tool is created. Tests to demonstrate the effectiveness of this approach and the optimal machining parameters are performed, and an example of the small and complex features that this new micro-machining

technique is capable of achieving is also presented. Finally, a comparison between the previous achievements and this new approach's characteristics is presented to justify its application.

4.2 Methodology

Conventional scale milling requires a cutting tool, a sample, and a machine that provides the necessary relative displacement between the cutting tool and the sample. Usually this displacement is divided in two different motions. The first one consists of the tool rotation that provides the cutting force, and the second is the one provided by the positioning system that moves the sample to create the desired features.

In this new approach, the same basic idea is applied. Tungsten probe tips with 1 um diameter are used as cutting tools, and mirror finished 10 x 10mm. aluminum sheets are used as work pieces. First of all, the tool is mounted on a tool holder (*Starret Pin Vase)*, and it is attached to the Z axis of a X, Y, Z digital automation platform (A 3200 Npaq). The tool is kept static during each cycle, and it is moved only parallel to the Z axis to provide the required depth of cut. The sample is mounted on the previously developed nano-positioning system to provide the tool-sample relative "rotation" through a circular path displacement provided by the nano-positioning stage. This whole assembly (the sample on the nano-positioning stage) is attached to the X, Y axes of the micro-positioning platform, which provides the necessary displacement in these directions to create the required features. The X, Y and Z displacements are controlled through numeric control (CNC) using the provided controller

for the automation platform, and the rotation like displacement is controlled through varying the voltage and phase of the sinusoidal signals applied to the two piezoelectric actuators attached to each axis of the nano-positioning system.

In this way, the sample can be moved as desired using the controller to create the required features. The micropositioning system provides a circular path relative displacement between the sample and the tool, so the tip and nano-positioning system assembly acts as a single tooth micro-milling tool with a minimum diameter of a few microns (depending on the applied voltage and tip diameter) mounted on a spindle that can achieve rotation speeds as high as 360.000 rpm. This approach is similar to fly cutting at conventional scales, but uses the nano-positioning stage instead of the conventional rotational spindle to generate the sample-tool relative motion. This configuration allows the achievement of features between several nanometers to a few microns with good accuracy, high efficiency and relatively low cost.

4.3 Set up and practical considerations

The basic set up for this experiment is similar to any conventional milling process set up. First of all, the tool must be fastened to the Z axis of the positioning table. To do this, a *Starret Pin Vase* tool holder capable of holding tools as small as several microns in diameter is used, and then, this holder is fastened to the Z axis of the table using two aluminum pieces held by screws. After that, the sample must be firmly fastened to the nano-positioning stage using a set of screws. This step requires special care due to the small size of the screws (M

1.6). Then, the sample nano-positioning assembly is attached to the automation platform using another set of screws. Finally, the zero set up is performed using a NAVATAR I-6265 zoom lens attached to a digital Unibrain microscopic video camera to visually approach the tip, and a multimeter to detect the final contact with the sample. A picture of the assembled system is presented in Figure 23.

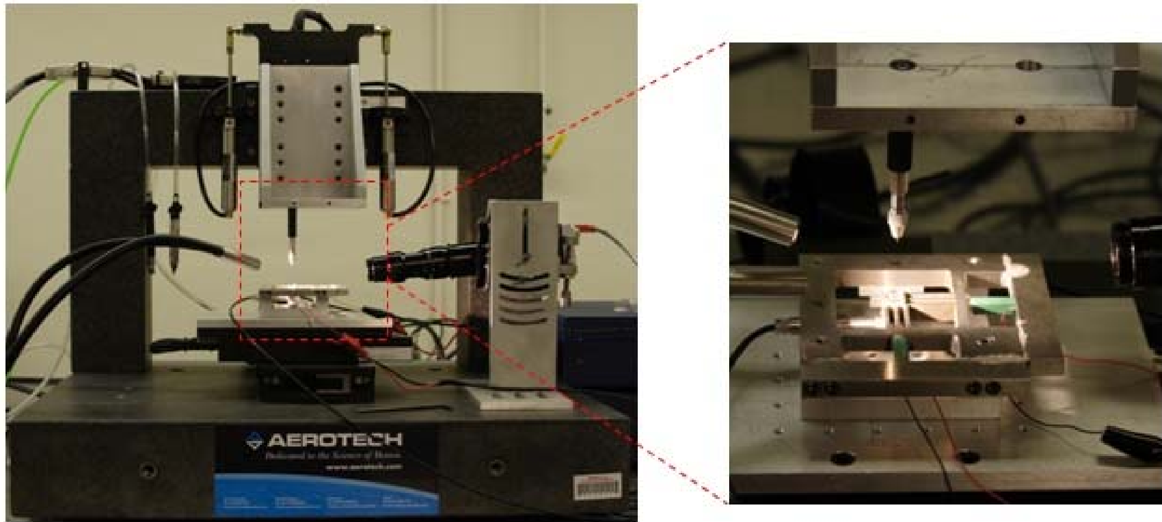

Figure 23: Set up for the proposed micro machining process.

The X and Y zero setup is performed manually trying to be as close as the sample center as possible in order to assure the best possible surface quality and flatness. At this point, this step is not of vital importance because the position of the machined features in the sample is not critical. For this reason, a visual localization of the tip is performed, and a final adjustment using the microscopic camera is accomplished. However, the Z position of the tip relative to the sample is extremely important, because the depth of cut cannot exceed under

any circumstances the tip radius. As it was told, the used tip radius is around 500 nm, so the approaching process must be made with extremely carefulness to avoid damaging the tip. For this reason, this approaching process is divided in three steps.

The first step is similar to the one used to localize the tip in the X and Y axes, it is, a visual approach until the tool is safely close to the sample. When the tip is as close as possible to the sample using this approach, the digital video camera with a magnification factor of 393 X is used to continue the approaching process. In this step, an extremely low approaching speed (around 100 nm/sec) is used to assure the integrity of the tip. This is done using the CNC control. The final step is a step by step approaching process using an even slower speed (50 nm/sec) and a 50 nm step. The multimeter is then used to detect the tool-sample contact through measuring the electrical resistance between the sample and the tip. When the tip touches the sample, this resistance is close to zero, so the step by step process is continued until the reading in the multimeter is close to zero. Through this process, a maximum tip-sample engagement of less than 50 nm is guaranteed for the first pass. Despite of this fact, because of the lack of the sample total flatness, sometimes the first pass can have more than 500 nm of engagement, producing damage to the tip and future problems to the surface finish and accuracy of the whole process.

In order to avoid this possibility, an alternative to this last step (Z approaching process) is presented. The alternative consists of adding some scanning steps to the used CNC G-CODE program before the first pass of the desired features. Using this approach, all the working surface is scanned in the previous steps before the tip is engaged to the sample (while the tip

is in the air but very close to the sample). Then, if there is a higher point in that surface, it will be machined before the others, thus ensuring a maximum engagement equal to the chosen Z step, which must be less than the previous mentioned tip radius. Using this approach, the tip integrity and the best possible surface finish are ensured.

To provide the necessary tool-sample displacement, a National Instruments data acquisition system (NI USB-6259 M SERIES) connected to a conventional PC is used. Using this equipment, two equal magnitude but different phase sinusoidal signals are sent through two piezoelectric amplifiers as actuation signal to the two axes piezoelectric actuators of the system. Varying the voltage and frequency, the circular path diameter and the angular velocity are changed and can be successfully controlled. The same system allows the user to control the resulting motion using capacitance sensor. In this way, changes in tool path can be recorded and further correction can be made to optimize the system's behavior.

4.4 Machining variables calculations

In this point as in the previous one, the parameters that are subject to modification are similar to the commonly used in conventional scale machining. Spindle speed, which in this approach's case is comparable to vibration frequency of the nano-positioning system over a circular path, feed rate and feed per tooth are the three main parameters that can be chosen to set the optimal combination for better surface finish and accuracy. In addition, since in this approach the tool is not rotating, the peak to peak vibration amplitude (V_{pp}) of the nano-positioning stage (i.e. the diameter of the circular path) is another important parameter that

can be controlled in this new technique, and its variation is equivalent to a different tool diameter in conventional scale machining through the relation expressed in equation 4.1.

$$T_d = V_{pp} + d_t \tag{4.1}$$

where T_d is the virtual tool diameter and d_t is the diameter of the used tip.

The depth of cut is also controlled through the Z displacement of the tool, as in a conventional milling process.

These parameters can be controlled using the basic set up in the CNC G-CODE programs and the vibration parameters (signals' frequency, phase and amplitude) of the nano-positioning system. Spindle speed is directly related with vibration frequency in kHz. This vibration frequency (V_f) in combination with the linear speed, that in this case defines the feed rate in mm/sec, determine the feed per tooth in um/rev as follows:

$$F_t = \frac{feed\ rate}{V_f} \tag{4.2}$$

This equation is valid because the system behaves as a single tooth tool milling process. The feed per tooth must be kept under the tip radius value to ensure good results.

Due to the small dimensions used in this process, the concept of removal rate is changed for the unit removal (UR) as defined in [48], it is the part of a work piece that is removed in one cycle of the machining process. For the presented process, this value will have units of area that can be changed to volume multiplying for the depth of cut.

$$UR = \frac{3r\pi F_t}{4} \tag{4.3}$$

where r is defined as the vibration amplitude (A) plus the tip radius. The parameters' combinations to obtain optimal results are material dependant. In the next section, a summary of experiments using aluminum samples (5052 alloy) are presented and the results are analyzed for further recommendations.

4.5 Experiments results

The first set of experiments was devoted to obtain satisfactory microscopic visual results in surface quality. The final judgments were performed based on digital pictures taken using an Olympus BHM metallurgical microscope (400 X maximum magnification factor) with a Paxcam digital microscope camera connected to a PC. To do so, Picoprobe ST-20-05 tungsten tips with diameter equal to 1 um were used as cutting tools and square 5052 aluminum pieces of 1 cm size were used as samples. Due to the specific aluminum alloy characteristics, the general propose *Tap Magic* cutting fluid was added to the process based on literature recommendations [49]. The machining parameters were then changed systematically to compare the obtained results. The different parameter combinations used for these visual surface quality tests are summarized in Table 2: Parameters combinations for visual surface quality tests..

From these combinations, the ones involving frequencies over 4 kHz and circular path diameters over 2 um could not be performed due to the shrinking effect in the nano-

positioning stage motion. It is, the maximum voltage was not enough to produce the required amplitude at those frequencies.

Table 2: Parameters combinations for visual surface quality tests.

Parameter	Initial value	Final Value	Increment
Vibration frequency (kHz)	0.50	6.00	0.50
Feed per tooth (um/rev)	0.10	0.50	0.05
Circular path diameter (um)	2.00	4.00	0.50

The combinations involving 0.5 kHz vibration frequency and feed per tooth less than 0.25 did not produced good results because these speed-feed rate combinations were not enough to form a chip during the cutting process, producing then the base material to melt and the surface quality to degrade.

All other combinations produce relatively equal surface quality, being barely appreciable a better results when higher vibration frequencies and feeds per tooth were used. A microphotography of the obtained results using 4 kHz and 0.25 um/rev configuration is presented in Figure 24.

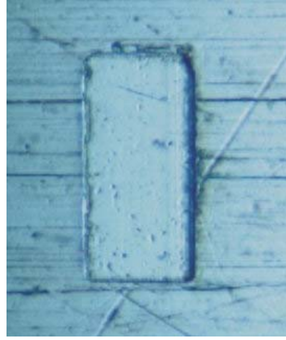

Figure 24: Achieved surface finish compared with mirror like (#8).

The second set of experiments was developed to verify the capacity of this new approach to produce small features. To do so, a G-CODE program was written to generate the tool path to write the word ISE. The tool path was generated considering different sectors, and in each sector, a circular clockwise tool path was considered decreasing systematically the diameter to cover the entire surface. A scheme of the used tool path is presented in Figure 25.

Using this program, the same set of parameter combinations were used, and the best results were obtained using 4 kHz and 0.25 um/rev combination. The tool vibration amplitude (circular path diameter) was 2 um, and each line in the tool trajectory showed in Figure 25 (a) is separated by 1 um.

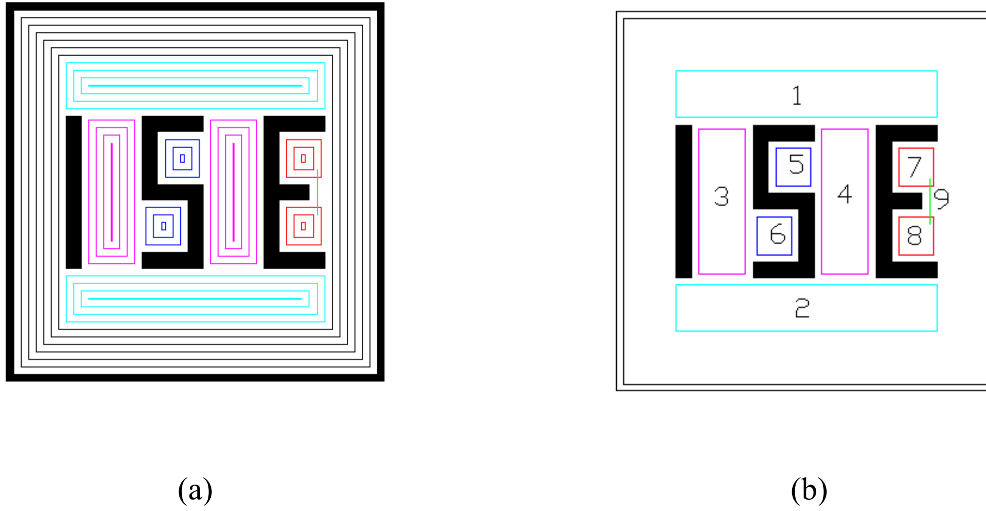

(a) (b)

Figure 25: Tool trajectory used in the G-CODE program. (a) Total surface trajectory. (b) Different considered sectors.

These results demonstrate the process capacity of generating features in the order of a few microns or less with good accuracy as shown in Figure 26.

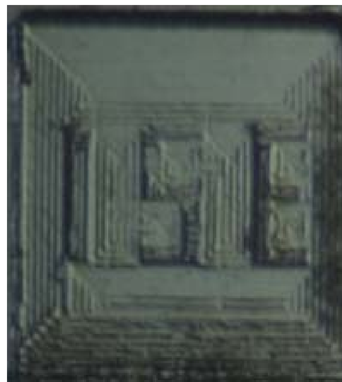

Figure 26: 2 x 10 um letters in a 50 um size square machined in aluminum using tungsten tip.

Another example, where less than a micron features can be observed, is shown in Figure 27.

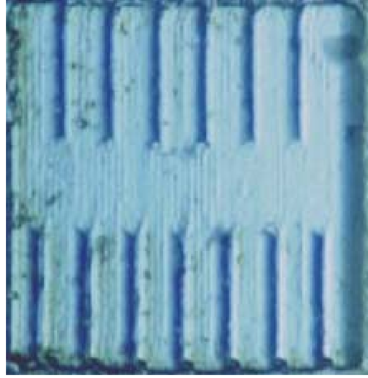

Figure 27: Array of half micron lines in a 50 um square.

The only two parameters that limit the minimum feature size are the tip diameter and the minimum achievable circular path diameter, which for the used nano-positioning system is around 10 nm. Since the commercially available tungsten tip sizes are in the order of hundreds of nanometers, the tip diameter is the limiting factor for internal features. If no internal features are required, the size is limited by the control over the vibration amplitude and the system's noise. The system's noise is in the order of a few nanometers, and since the system can operate under closed-loop conditions, the machining approach has potentially the ability of producing features as small as a few nanometers.

4.6 Conclusions

The new designed machining approach is a practical application of the previously developed nano-positioning system. This new process consists of a 1 um tungsten tip attached to the Z axis of an automation motion platform and an assembly of the previously designed nano-positioning stage and the sample to be machined attached to the X, Y axes of that platform.

The nano-positioning stage provides de required tool-sample relative motion, and the platform moves the system to create the desired features. Comparing with conventional size milling parameters, the nano-positioning system provides the spindle speed, while the platform acts as the X, Y and Z motion axis.

This configuration was proven to be able to achieve good surface quality and to produce features in the nanometer level range. The presented results are limited to tungsten tips and specific alloy aluminum samples, but with the achieved speeds and accuracies, the technique can be used to machine almost any material, and could achieve smaller features if a smaller diameter tip is used. The surface quality can also be potentially improved using diamond tips instead of tungsten ones. The parameter combinations will vary depending on the tip and sample materials, but the achieved accuracy will be kept constant. It can be even improved using a closed-loop control system for the nano-positioning stage vibration, as mentioned before. Finally, the new machining system has the potential to be applied in different industries, such as precise optics and MEMS.

CHAPTER 5: Conclusions and recommendations

In this document, a successfully designed new nano-positioning module, a 2 DOF nano-positioning stage and a possible micro-machining application using this stage are presented, implemented and tested. Previous work done in these fields has been revised to verify the validity of the current research. Theoretical analyses were developed to understand the module and system behavior. Then, FEM analyses were used to test and verify the module and system response to simulated loads and vibration modes. Finally, experimental results were obtained from the nano-positioning system, and a practical specific micro-machining application was developed and tested.

In chapter two, a hybrid nano-positioning module is presented and tested through FEM. The module combines the two broadly used concepts of lumped-compliance flexures (hinges based) and distributed-compliance flexures (beam based), proposing a hybrid system that decouples the two sought characteristics: high bandwidth and low parasitic error. The proposed configuration achieves higher natural frequency (bandwidth) than the previously developed ones, and parasitic errors as low as the best previously proposed. In addition, this design permits choosing the hinges and beams dimensions to achieve the required performance without altering the global good behavior. It is, when the bandwidth is scaled up through increasing the beams' size, the parasitic motion can be kept low adjusting the hinge's size.

In chapter three, a combination of two of these modules in a parallel configuration is presented to design a new 2 DOF nano-positioning stage. Two additional doubly-clamped beams parallel to each module are added to provide additional stiffness to the system and to act as prismatic joints in conjunction with piezoelectric actuators. This design decouples the X and Y motion and provides the same advantages of high bandwidth and low parasitic motion that its component modules provide. These characteristics are confirmed through theoretical static and dynamic analyses and FEM analysis. The system is then built and tested to demonstrate its characteristics. A maximum workspace of 15 um per size is found, as well as 8 kHz open loop bandwidth. These characteristics represent a good improvement for applications that requires high bandwidth and good accuracy of motion, such as microscope scanners and micro-manufacturing applications. Moreover, the nano-positioning stage is integrated in a closed-loop control system, and it proved to be able to behave accordingly to the required high bandwidth and accuracy for its possible applications.

Chapter four describes a new approach for micro-milling, using the previously designed nano-positioning system to replace the traditional spindle used in conventional milling process. This different configuration allows the users to achieve rotational speed over 360.000 rpm, which is not possible with conventional milling or turning machines. The process consists of mounting an static tool attached to the Z axis of a automation platform, and mounting the nano-positioning stage with the sample on the X, Y axes. Then, the nano-positioning system provides the required tool-sample displacement over a circular trajectory, and the automation platform moves the system go create the desired features. This new

configuration demonstrated to be able to machine features in the nanometer level range, as well as obtaining good surface quality, when the right combination of parameters, sample materials and tips are chosen. Further work need to be done to optimize this approach, but the current results verify that the system can achieve good results with high speed and relative low cost.

In conclusion, a 1 DOF nano-positioning module was designed and tested for high bandwidth and low parasitic motion. Then, a 2 DOF nano-positioning stage was developed using the previously designed modules as building blocks. This system was also tested to demonstrate high bandwidth, low Abbe/sine error, and good accuracy. In addition, it was integrated to a closed-loop system to control the displacement and improve the accuracy. Finally, the developed system is integrated to a new approach of micromachining, taking the place of the traditional spindle in conventional scale machining. The new approach is tested, and the good accuracy and high speed of the process are demonstrated. Further recommendations for possible improvements to the system are finally introduced to propose a continuous field of research.

REFERENCES

1. *Tool tip trajectories investigation and its influences in micromilling operation.* **Yadong Gong, Jinsheng Wang, Gabriel Abba, Jean Francois Antoine, Jiashun Shi.** s.l. : IEEE, 2008. pp. 440-445.

2. **Winston, Wayne L.** *Operations Research.* NY : PWS-Kent, 1991. 0-534-98079-1.

3. *Notch Flexure Hinges: An effective theory.* **Tseytlin, Y.M.** 9, s.l. : Review of Scientific Instruments, 2002, Vol. 73, pp. 3363-3368. 10.1063/1.1499761.

4. *Microstructure grooves with a width of less than 50 um. cut with ground hard metal micro end mills.* **Th. Schaller, L. Bohn, J. Mayer, K. Schubert.** s.l. : Precision Engineering, 1999, Vol. 23, pp. 229-235.

5. *Effects of AFM-based nanomachining process on aluminum surface.* **T. Fang, W. Chang.** s.l. : Journal of Phisics and Chemistry of Solids., 2003, Vol. 64, pp. 913-918.

6. *Micromachining by CNC Slotting Using a Steered Tool.* **Schaller Th, Schubert K.** s.l. : ASPE 16th Annual Meeting, 2001. pp. 469-472.

7. *A precision piezodriven micropositionermechanism with large travel range.* **S.H. Chang, B.C. Du.** 4, s.l. : Review of Scientific Instruments, 1998, Vol. 69, pp. 1785-1791.

8. *High-Bandwidth Nano-Positioning Modules for High-throughput Micro/Nano Manufacturing.* **S. Polit, J. Dong.** Miami : s.n., 2009. 2009 Industrial Engineerign Research Conference. pp. 1-6.

9. *Elastic Averaging in Flexure Mechanisms: A Multibeam Parallelogram Flexure Case-Study.* **S. Awtar, E. Sevincer.** 2006.

10. *Characteristics of Beam-based Flexure Modules.* **S. Awtar, A.H. Slocum, E. Sevincer.** s.l. : Journal of Mechanical Design, 2007, Journal of Mechanical Design, Vol. 129, pp. 625-639.

11. *Design and characterization of a low-profile micropositioning stage.* **R. Yang, M. Jouaneh, R. Schweizer.** s.l. : Precision Engineering, 1996, Vol. 18, pp. 20-29.

12. *Design, analysis, fabrication and testing of a parallel-kinematic micropositioning XY stage.* **Qing Yao, J. Dong, P. M. Ferreira.** 2007, International Journal of Machine Tools & Manufacture, pp. 946-961.

13. —. **Q. Yao, J. Dong, P. M. Ferreira.** s.l. : International Journal of Machine Tools & Manufacture, 2007, International Journal of Machine Tools & Manufacture, Vol. 47, pp. 946-961.

14. *A Novel Parallel Kinematics mechanisms for Integrated, Multi-axis Nano-positioning. Part1: Kinematics and Design for Fabrications.* **Q. Yao, J. Dong, P.M. Ferreira.** 1, s.l. : Precision Engineering, 2008, Vol. 32, pp. 7-19.

15. *Nanomachining of Silicon Surface Using Atomic Force Microscope With Diamond Tip.* **N. Kawasegi, N. Takano, D. Oka, N. Morita, S.Yamada, K. Kanda, S. Takano, T. Obata, K. Ashida.** 723, s.l. : Journal of Manufacturing Science and Engineering., 2006, Vol. 129.

16. **Lobontiu, Nicolae.** *COMPLIANT MECHANISMS Design of Flexure Hinges.* New York : CRC PRESS, 2002. ISBN 0-8493-1367-8.

17. —. *COMPLIANT MECHANISMS Design of Flexure Hinges.* New York : CRC PRESS, 2002. ISBN 0-8493-1367-8.

18. *Measurement of Milling Tool Vibrations During Cutting Using Laser Vibrometry.* **Kourosh Tatar, Per Gren.** s.l. : International Journal of Machine Tools & Manufacture, 2008, Vol. 48.

19. *Piezoelectrically driven XYθ table for submicron lithography systems.* **K. Sugihara, I. Mori, T. Tojo, C. Ito, M. Tabata, T. Shinozaki.** 9, s.l. : Review of Scientific Instruments, 1989, Vol. 60, pp. 3024-2029.

20. *Design and analysis of a micro-positioning module for multi-degree -of-freedom micro-positioners.* **Jingyan Dong, Young Hun Jeong, and Placid M. Ferreira.** 2007, ICOMM, p. # 38.

21. *Design, fabrication and testing of a silicon-on-insulator (SOI) MEMS parallel kinematics XY stage.* **Jingyan Dong, Deepkishore Mukhopadhyay and Placid M. Ferreira.** 2007, Journal of Micromechanics and Mircoengineering, pp. 1154-1161.

22. *Micropositioning device using solid state actuators for diamond turning machines: a preliminary experiment.* **J.C. Campos Rubio, J.G. Dubuch, A. Vieira Porto.** s.l. : Proceeding of SPIE - the International Society for Optical Engineering, 1997, Vol. 3044, pp. 317-326.

23. *Design and analysis of a micro-positioning module for multi-degree -of-freedom micro-positioners.* **J. Dong, Y. Hun Jeong, P.M. Ferreira.** s.l. : ICOMM, 2007. Vol. 38.

24. *A Novel Parallel-Kinematics mechanism for Integrated, Multi-axis Nano-positioning. Part 2: Dynamics, Control and Performance Analysis.* **J. Dong, Q. Yao, P.M. Ferreira.** 1, s.l. : Precision Engineering, 2008, Vol. 32, pp. 20-33.

25. *Electrostatically actuated cantilever with SOI-MEMS parallel kinematic XY stage.* **J. Dong, P.M. Ferreira.**

26. *Design, fabrication and testing of a silicon-on-insulator (SOI) MEMS parallel kinematics XY stage.* **J. Dong, D. Mukhopadhyay, P.M. Ferreira.** 6, s.l. : Journal of Micromechanics and Microengineering, 2007, Journal of Micromechanics and Mircoengineering, Vol. 17, pp. 1154-1161.

27. **I. Bonev.** http://www.parallemic.org/Reviews/Review002.html. *Delta parallel robot.* [Online]

28. **Howell, Larry L.** *Compliant Mechanisms.* New York : John Wiley & Sons, Inc., 2001.

29. —. *Compliant Mechanisms.* New York : John Wiley & Sons, Inc. , 2001.

30. **Hodgson, Thom.** *Production & Inventory Control.* Raleigh : Sir Speedy, 2008.

31. *Finite element analysis of a scanning x-ray microscope micropositioning stage.* **H.T.H. Chen, W. Ng, R.L. Engelstad.** 1, s.l. : Review of Scientific Instruments, 1992, Vol. 63, pp. 591-594.

32. *Estimation of cutting forces in micromilling through the determination of specific cutting pressures.* **H. Pérez, A. Vizán, J.C. Hernandez, M. Guzmán.** s.l. : Journal of Materials Processing Technology, 2007, pp. 18-22.

33. *Optimized flexural hinges for compliant Micromechanisms.* **GH.Munteanu, F. de Bona and M.** s.l. : Analog Integrated Circuits and Signal Processing, 2005, Vol. 44, pp. 163-174.

34. *Design and Modeling of a High-Speed AFM-Scanner.* **Georg Schitter, Karl J. Astrom, Barry E. DeMartini, Philipp J. Thurner, Kimberly L. Turner, Paul K. Hansma.** 5, September 2007, IEEE TRANSACTIONS ON CONTROL SYSTEM TECHNOLOGY, Vol. 15, pp. 906-915.

35. —. **Georg Schitter, Karl J. Astrom, Barry E. DeMartini, Philipp J. Thurner, Kimberly L. Turner, Paul K. Hansma.** September 2007, IEEE TRANSACTIONS ON CONTROL SYSTEM TECHNOLOGY, pp. 906-915.

36. *Recent Advances in Mechanical Micromachining.* **D. Dornfeld, S. Min, Y. Takeuchi.** s.l. : Annals of the CIRP, 2006, Vol. 55/2/2006, pp. 745-768.

37. *Effect of workpiece springback on micromilling forces.* **C. R. Friedrich, V. P. Kulkarni.** s.l. : Microsystem Technologies, 2004, pp. 472-477.

38. *Analysis and Design of Parallel Mechanisns Whith Flexure Joints.* **Byoung Hun Dang, John Ting-Yung Wen, Nicholas G. Dagalakis, Jason J. Gorman.** 2005, IEEE TRANSACTIONS ON ROBOTICS, pp. 1-6.

39. —. **B.H. Kang, J.T. Wen, N.G. Dagalakis, J.J. Gorman.** 6, s.l. : IEEE Transactions on Robotics, 2005, IEEE TRANSACTIONS ON ROBOTICS, Vol. 21, pp. 1179-1185.

40. *Femtosecond laser aperturless near-field nanomachining of metals assisted by scanning probe microscope.* **A. Chimmalgi, T. Y. Choi, C. P. Grigoropoulos, K. Komvopoulos.** 8, s.l. : Applied phisics letters, 2003, Vol. 82.

41. *Development of a compact high-load PZT-ceramic log-travel linear actuator with picometer resolution for active optiical alignment applications.* **Marth, H. and Lula, B.** s.l. : Proceedings of SPIE: Optomechanical Technologies for Astronomy, 2006. Vol. 6273 I.

42. *A chronic micropositioning system for neurophisiology.* **Muthswamy, J. Salas, D. Okandan, M.** s.l. : Annual International Conference of the IEEE Engineering in Medicine an Biology, 2003. Vol. 3, pp. 2115-2116.

43. *High-speed solution switching using piezo-based micro-positioning stages.* **Stilson, S. McClellan, A. Devasia, S.** s.l. : Proceedings of the American Control Conference, 2001. Vol. 3, pp. 2238-2243.

44. *Design of a low-cost nano-manipulator wich utilizes a monolithic, spatial compliant mechanism.* **Culpepper, M.L. Anderson, Gordon.** s.l. : Precision Engineering, 2004. Vol. 28, pp. 469-482.

45. *True atomic resolution by atomic force microscopy through repulsive and attractive forces.* **Ohnesorge, F. Binning, G.** 5113, s.l. : Science, 1993, Vol. 260, pp. 1451-1456.

46. *Surface studies by scanning tunneling microscopy.* **Binnig, G. Rohrer, H. Gerger, Ch. Weibel, E.** 1, s.l. : Physical Review Letters, 1982, Vol. 49, pp. 57-61.

47. *Tunneling through a controllable vacuum gap.* **Binnig, G. Rohrer, H. Gerber, Ch. Weibel, E.** 2, s.l. : Applied Physics Letters, 1982, Vol. 40, pp. 178-180.

48. **Meyer, E. Hug, H.J. Bennewitz, R.** *Scanning Probe Microscopy: The Lab on a Tip.* 1. s.l. : Springer, 2003.

49. *Dip-Pen Nanolithography.* **Piner, R.D. Zhu, J. Xu, F. Hong, S. Markin, C.A.** 5402, s.l. : Science, 1999, Vol. 283, pp. 661-663.

50. *Polymer Pen Lithography.* **Huo, F. Zheng, Z. Giam, L.R. Zhang, H. Mirkin, C.A.** s.l. : Science, 2008, Vol. 321, pp. 1658-1660.

51. *Protein nanoarrays generated by dip-pen nanolithography.* **Lee, K-B. Park S-J. Mirkin, C.A. Smith J.C. Mrksich, M.** s.l. : Science, 2002, Vol. 295, pp. 1702-1705.

52. *How to design flexure hinges.* **Paros, J.M. Weisbord, L.** s.l. : Machine design, November 1965, pp. 151-156.

53. *5-axis micro milling machine for machining micro parts.* **Young-bong Bang, Kyung-min Lee, Seungryul Oh.** 9-10, s.l. : The International Journal of Advanced Manufacturing Technology. , 2005, Vol. 25.

54. *Micro milling of pure copper.* **M. Rahman, A. Senthil Kumar, J.R.S. Prakash.** 1, s.l. : Journal of Materials Processing Technology, 2001, Vol. 116.

55. *Current status in, and future trends of, ultaprecison machining and ultrafine materials processing.* **Taniguchi, N.** 2, s.l. : Annals of the CIRP, 1983, Vol. 32.

56. *Nanotechnology: International developments and emerging products.* **J. Corbett, P.A. McKeown, G.N. Peggs, R. Whatmore.** 2, s.l. : Annals of the CIRP, 2000, Annals of the CIRP, Vol. 49, pp. 523-545.

57. *State of the art of micromachining.* **Masuzawa, T.** 2, s.l. : Annals of the CIRP, 2000, Vol. 49, pp. 473-488.

58. *Development of a compact high-load PZT-ceramic long-travel linear actuator with picometer resolution for active optical alignment applications.* **B., Math H. and Lula.** s.l. : Proceeding of SPIE: Optomechanical Technologies for Astronomy, 2006, Vol. 6273.

59. *Atomic Force Microscope.* **Binnig, G. Quate, C.F. Gerber, Ch.** 9, s.l. : Physical Review Letters, 1986, Vol. 56, pp. 930-933.

60. *A mechanical microscope: High speed atomic force microscopy.* **A.D.L. Humphris, M.J. Miles, J.K. Hobbs.** s.l. : Applied Physics Letters, 2005, Vol. 86.

61. *A high-speed atomic force microscope for studying biological macromolecules in action.* **T. Ando, N. Kodera, D Maruyama, E. Takai, K. Saito, A. Toda.** s.l. : Jpm. J. Appl. Phys., 2002, Vol. 41.

62. *High resonance frequency force microscope scanner using inertia balance support.* **T. Fukuma, Y. Okazaki, N. Kodera, T. Uchihahsi, T. Ando.** s.l. : Appl. Phys. , 2008, Vol. 92.

63. *High-speed serial-kinematic SPM scanner: Design and drive considerations.* **K.K. Leang, A.J. Fleming.** s.l. : American Control Conference, 2009. Vol. 11.

64. *Constrint-based design of parallel kinematic XY flexure mechanisms.* **S. Awtar, A.H. Slocum.** 8, s.l. : ASME Journal of Mechanical Design, 2007, Vol. 129.

65. *A SOI MEMS-based 3-DOF planar parallel-kinematics nanopositioning stage.* **D. Mukopadhyay, Jingyan Dong, Eakkachai Pengwang, Placid Ferreira.** 1, s.l. : Sensors and Actuators A: Physical, 2008, Vol. 147.

66. *Micropositioning device for automatic alignment of substrates for industrial-scale thin films deposition.* **A. Castañeda, L.M. Apatiga, R. Velazquez, V.M. Castano.** 4, s.l. : Assembly Automation, 2001, Vol. 21, pp. 336-340.

67. http://www.metalsuppliersonline.com/Research/Property/metals/472.asp. *Metal suppliers online.* [Online] Metal suppliers online. [Cited: Dec 13, 2009.]

68. *Design and analysis of a totally decoupled flexure-based XY parallel micromanipulator.* **Y. Li, Q, Xu.** 3, s.l. : IEEE Transactions and Robotics, 2009, Vol. 25.